The Thesis Committee for Matthew Jeffrey Horner
Certifies that this is the approved version of the following thesis:

Experimental and Computational Investigation of Turbine Cooling Designs Incorporating a Thermal Barrier Coating

APPROVED BY

SUPERVISING COMMITTEE:

David G. Bogard, Supervisor

Todd A. Oliver

Experimental and Computational Investigation of Turbine Cooling Designs Incorporating a Thermal Barrier Coating

by

Matthew Jeffrey Horner

THESIS

Presented to the Faculty of the Graduate School of

The University of Texas at Austin

in Partial Fulfillment

of the Requirements

for the Degree of

MASTER OF SCIENCE IN ENGINEERING

THE UNIVERSITY OF TEXAS AT AUSTIN

December 2020

Dedication

To Mom and Dad. Thank you for everything.

Acknowledgments

I would like to thank Dr. David Bogard for his guidance and dedication throughout my graduate studies. He has pushed me to grow as an engineer, and the wisdom he has shared with me has been invaluable. Thank you as well to Dr. Todd Oliver for his guidance in computational analysis.

I would also like to thank my TTCRL colleagues, who were a valuable part of my graduate school experience. Thank you to Jacob Moore for his mentorship early on, both as a researcher and as a teaching assistant. Thank you to Fraser Jones for the countless hours spent troubleshooting CFD issues, and to Dale Fox for his guidance in experimental methods. A big thank you goes to Chris Yoon and Michael Furgeson for many late nights spent in the lab assembling our test section and running experiments. The animated white board discussions and Fridays at Crown will be missed.

Thank you to my friends and family for their support during graduate school. I could not have done it without you.

Abstract

Experimental and Computational Investigation of Turbine Cooling Designs Incorporating a Thermal Barrier Coating

Matthew Jeffrey Horner, M.S.E.
The University of Texas at Austin, 2020

Supervisor: David G. Bogard

Few studies in the open literature have investigated the effect of thermal barrier coatings (TBC) on gas turbine component thermal protection designs. The current study evaluated shaped hole film cooling and internal cooling enhanced with rib turbulators separately as well as part of an integrated design incorporating a TBC. The design and construction of a matched-Biot number test section is discussed along with an evaluation of uncertainty. Enhanced internal cooling was found to provide a 44% increase in overall effectiveness without a TBC. The TBC provided a 47% increase in spatially-averaged effectiveness on the metal-TBC interface. The optimum velocity ratio with a TBC was shown to be lower than that without a TBC as the internal cooling effects were reduced with the extraction of coolant. A RANS conjugate heat transfer study closely predicted the performance of the configurations tested without a TBC, but over-predicted the effectiveness of designs incorporating a TBC.

Table of Contents

List of Tables

List of Figures

Chapter 1

Introduction

This chapter provides an introduction to gas turbine engines and the thermodynamics that govern their operation as the motivation for this work. Thermal protection mechanisms for turbine hot gas path components will be discussed followed by a review of relevant studies in the open literature.

1.1 Gas Turbine Engines

Gas turbine engines drive our world, from military and commercial aircraft propulsion to electric power generation. In 2018, the U.S. Energy Information Administration estimated that gas turbine power plants made up 38.4% of domestic power generation, at over one trillion kilowatt-hours [1]. In 2019, gas turbine engines powered over 32,000 aircraft worldwide, with this number expected to grow by 1.8% annually in the coming decades [2]. Due to their widespread usage across both the transportation and power generation sectors, small increases in efficiency can yield large benefits in the form of reduced operating costs and emissions.

1.1.1 Brayton Cycle Thermodynamics

The gas turbine engine operates on the Brayton thermodynamic cycle, which has three main components: the compressor, the combustor, and the turbine. Figure 1.1 shows a schematic of this process, while Figure 1.2 shows a detailed view of these components. From left to right, the multi-stage compressor incrementally increases the air pressure, then fuel is injected into the high-pressure gas flow and ignited. The hot gas, which can reach temperatures of 2200K, is accelerated by a static vane before passing through the rotating turbine stage [3]. The turbine stage is coupled to the compressor shaft and a portion of the turbine work output is used to drive the compressor and maintain the cycle.

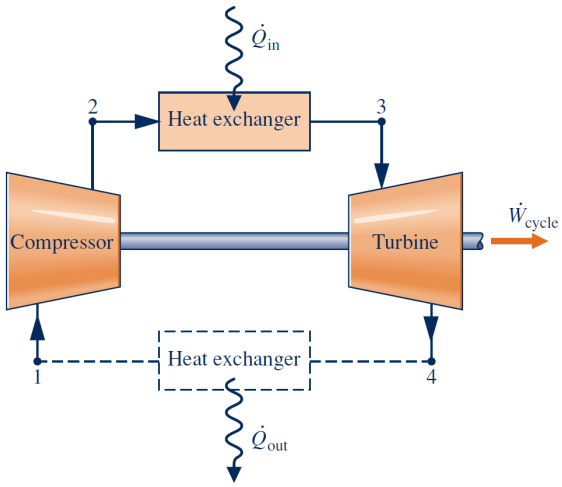

Figure 1.1: Schematic of a Brayton cycle engine [4].

An analysis of Brayton cycle thermodynamics shows that the thermal efficiency of the engine depends on the temperature at each stage as shown in Equation 1.1:

$$\eta_{Brayton} = \frac{\dot{W}_{net}}{\dot{Q}_{in}} = 1 - \frac{T_4 - T_1}{T_3 - T_2} \tag{1.1}$$

The thermal efficiency is a measure of the fraction of the fuel energy content that is converted to a useful work output, with the remainder being lost to heat and friction.

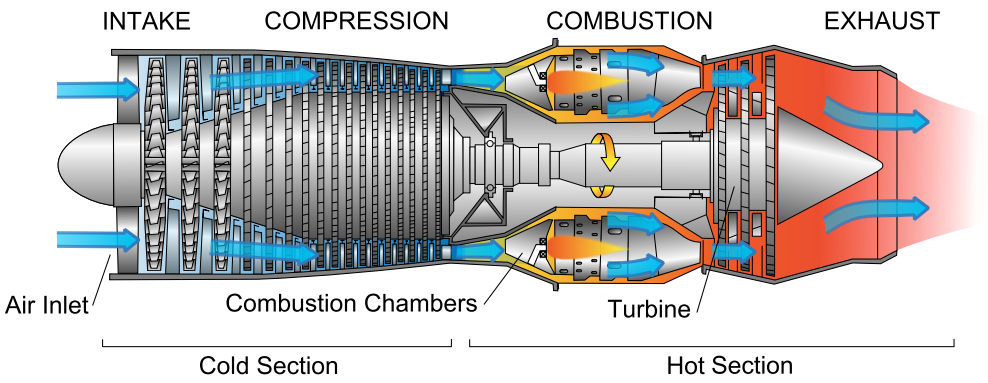

Figure 1.2: Components of a typical gas turbine engine [5].

The rate of heat addition $\dot{Q}_{in}$ is directly related to the rate of fuel consumed by the engine, and thus it is advantageous to raise the thermal efficiency to reduce fuel consumption. The inlet temperature T_1 is a function of the operating environment and T_2 is a function of the pressure ratio across the compressor as described in the following equation:

$$T_2 = T_1\left(\frac{P_2}{P_1}\right)^{\frac{\gamma-1}{\gamma}} \tag{1.2}$$

Similarly, the exhaust temperature T_4 is a function of the pressure ratio and the turbine inlet temperature T_3:

$$T_4 = T_3\left(\frac{P_1}{P_2}\right)^{\frac{\gamma-1}{\gamma}} \tag{1.3}$$

In these equations, γ is the ratio of specific heats of the working fluid.

For an ideal cycle, the turbine designer has control over the compressor pressure ratio and the turbine inlet temperature as a means of increasing thermal efficiency and work output. Further analysis shows that the maximum work output per unit mass is a function of T_3:

$$\left.\frac{\dot{W}}{\dot{m}}\right|_{max} = c_p T_1 \left[\frac{T_3}{T_1} - 2\sqrt{\frac{T_3}{T_1}} + 1\right] \tag{1.4}$$

Clearly, the main driver of gas turbine specific work output is the turbine inlet temperature (TIT). It has long been a goal of engine designers to raise this as high as possible, although metallurgical constraints of the components in the hot gas path (HGP) limit the maximum temperature that can be obtained. In addition to the development of superalloys that can withstand elevated temperatures without softening beyond allowable limits, cooling schemes have been developed that actively cool the HGP components and allow the engine to operate above the components' material limits. This is done by diverting relatively cooler air from the compressor around the combustor to internal passages inside the turbine blades and vanes. Figure 1.3 shows the progression of commonly used cooling schemes for Pratt & Whitney engines. It should be noted that the air used for cooling the HGP components requires work input to raise the pressure and produces no useful work output. As a result, improving the effectiveness of cooling technologies has been a major research area since the 1960's and has enabled advanced airfoil designs.

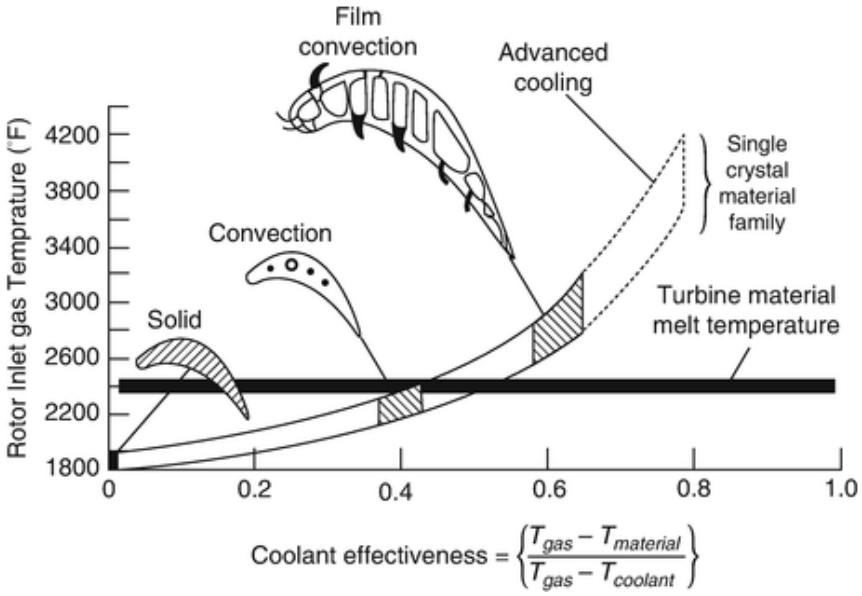

Figure 1.3: Pratt and Whitney turbine airfoil cooling design evolution [6].

1.2 Internal Cooling

1.2.1 Fundamentals of Internal Convective Cooling

In order to protect the airfoil and ensure that it meets its designed service life, the internal cooling system must be able to maintain the metal temperature below the maximum allowable temperature for each point on the component. As the heat load varies between different regions of the airfoil, the cooling system may use a variety of techniques at each location. For example, the leading edge is subject to a significant heat load due to the presence of a stagnation point and the thinner boundary layer on the suction side increases heat transfer to the metal surface.

The heat load Q that the coolant absorbs is defined in Equation 1.5, where h_i is the internal heat transfer coefficient, A is the wetted surface area, T_m is the surface

temperature, and T_b is the bulk coolant temperature.

$$Q = h_i A(T_m - T_b) \tag{1.5}$$

Common heat transfer enhancement mechanisms such as rib turbulators or pin fins have the dual benefit of increasing both h_i and A and leading to an increased cooling effectiveness. In order to scale heat transfer characteristics between different geometric scales and operating conditions, the convective heat transfer coefficient h is often reported as the nondimensional Nusselt number Nu:

$$Nu = \frac{h_i D}{k} \tag{1.6}$$

In Equation 1.6, D is the characteristic length scale (typically the hydraulic diameter D_h for internal flow) and k is the thermal conductivity of the fluid. Similarly, the friction factor f is used to quantify pressure drop for different geometries as defined in Equation 1.7, where ρ is the fluid density and V is the velocity in the channel.

$$\Delta P = f\Big(\frac{L}{D}\Big)\frac{\rho V^2}{2} \tag{1.7}$$

While elevated turbulence levels are known to increase convective heat transfer in internal channels, a greater pressure drop is required for a given length of channel. As the coolant is diverted from the compressor, there is a finite pressure driver available for the coolant system. In designing a coolant circuit, it is important to maintain a sufficient pressure margin to prevent hot gas ingestion into the airfoil. An important performance metric for internal cooling is the convective cooling efficiency as defined in Equation 1.8 [7]:

$$\eta_{conv} = \frac{T_{c,out} - T_{c,in}}{T_{metal} - T_{c,in}} \tag{1.8}$$

For peripheral cooling circuits located near the outer wall of the airfoil, the coolant is exhausted through film cooling holes well before η_{conv} approaches unity and the rate of heat transfer tends to zero. The engine designer must decide at what point to locate the film cooling hole such that the coolant will effectively pick up heat by convection before ejecting from film cooling holes [7].

1.2.2 Common Internal Cooling Techniques for Blades and Vanes

High pressure turbine vanes and blades employ a variety of different cooling techniques throughout their geometries, although the specific thermal design is a closely-guarded trade secret for most companies. First stage vanes, which are directly downstream of the combustor, typically use impingement jet arrays throughout [8]. First stage blades generally use a multi-pass serpentine channel, often with turbulators on the outer wall. Both components incorporate impingement and film cooling in the leading edge, where a stagnation point increases the local heat load to the part. Pin fins and slots are used in the thin trailing edge [8].

1.2.3 Additive Manufacturing Considerations

Additive manufacturing (AM) advances have enabled the construction of gas turbine components with geometries not previously possible with conventional manufacturing techniques. Specifically, direct metal laser sintering (DMLS) has expanded the design space of internal cooling designs to allow for complex winding ducts and a variety of channel shapes. Kirsch et al. [9] demonstrated a numerically optimized wavy channel design that improved heat transfer performance that would not be pos-

sible with conventional subtractive manufacturing techniques. These tools can be used to target hot spots on a component and improve the convective efficiency by increasing the surface area for a given channel cross-sectional area and controlling the features of the internal flow fields. The large surface roughness inherent to the AM build process is known to increase both heat transfer and friction factor in these internal channels [10]. Stimpson et al. [10] showed that the Nusselt number augmentation for rectangular engine-scale microchannels ($D_h \approx 0.6mm$) can be as high as 3.5x compared to a smooth duct of the same size as a result of AM roughness alone. Friction factor increase can be as high as 10x. AM roughness shows a similar effect on both pressure drop and heat transfer to turbulated channels and must be accounted for in the design process [8].

1.3 Film Cooling

1.3.1 Fundamentals of Film Cooling

Film cooling has been an important part of turbine thermal designs since its introduction in the 1950s [11]. Compressor bleed air is routed through internal passages in the airfoil before being exhausted through holes in the external wall of the airfoil. The goal of film cooling is to create a blanket of relatively cooler air over the external surface of the airfoil to reduce the driving temperature for heat transfer into the component surface. A schematic of a film cooling jet can be seen in Figure 1.4, in which coolant is injected into the flow from the hole at $x/D = 0$. The combustor discharge air flows from left to right at T_∞, and the wall is located at $y/D = 0$, where D is the diameter of the film cooling hole. The nondimensional temperature θ is used

to compare laboratory results to actual engine temperatures that can be an order of magnitude higher:

$$\theta = \frac{T_\infty - T}{T_\infty - T_c} \tag{1.9}$$

In the above equation, T_c is the coolant temperature at the exit of the hole. Typically, the adiabatic wall temperature T_{aw}, or the fluid temperature directly adjacent to a perfectly adiabatic wall, is used as the driving temperature for convective heat transfer to the metal at temperature T_m as follows:

$$q''_f = h_f(T_{aw} - T_m) \tag{1.10}$$

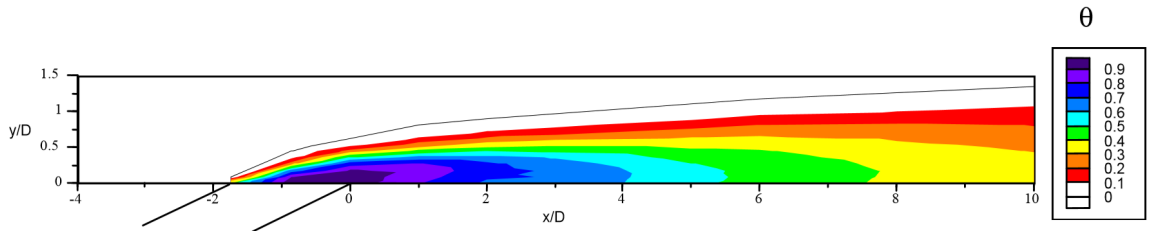

Figure 1.4: Nondimensional temperature θ profile of a film cooling jet, reproduced from [11].

The external heat transfer coefficient with film cooling, h_f, is typically greater than for the case without film cooling due to the addition of turbulence caused by momentum injection into the boundary layer. The performance of film cooling designs is often judged based on the ability to reduce the adiabatic wall temperature via the adiabatic effectiveness η:

$$\eta = \frac{T_\infty - T_{aw}}{T_\infty - T_{c,exit}} \tag{1.11}$$

In the above equation, $T_{c,exit}$ refers to the temperature of the coolant at the exit of the hole in order to account for warming effects through the bore of the

hole. Measurements of adiabatic effectiveness capture the thermal footprint of the jet on the component surface. Although the "adiabatic wall" is an ideal case that is approximated in laboratory settings, real engine components have a conductive metal wall that allows for the conjugate effects of internal cooling as well as external film cooling. The overall effectiveness parameter ϕ takes into account the contribution of both internal and film cooling in evaluating the integrated thermal design:

$$\phi = \frac{T_\infty - T_w}{T_\infty - T_{c,internal}} \tag{1.12}$$

The overall effectiveness parameter is dependent on the coolant temperature at the beginning of the coolant circuit, $T_{c,internal}$, which can be in the range of 750K depending on the engine pressure ratio [12].

One of the primary goals of film cooling designs in maintaining the jet attached to the component surface. If the jet were to separate from the surface, it no longer provides the film coverage required for cooling and introduces turbulent mixing that brings hot gas closer to the vulnerable metal, thus causing more harm than benefit to the airfoil. A major research area over the previous decades has been investigation of the film cooling hole geometry in order to increase the cooling efficiency and prevent jet separation.

1.3.2 Geometric Description of Film Cooling Holes

The earliest film cooling holes were cylindrical bores that could be drilled through the exterior wall of the airfoil. The holes are typically cut at an injection angle α that allows the flow to be more aligned with the mainstream as it exits the

hole. Shaped film cooling holes were introduced into commercial service around 1985 [8] and feature a diffuser-shaped expansion at the outlet of the hole. According to Ron Bunker at General Electric, shaped holes are widely regarded as "the most robust and reliable improvement in film cooling" due to their ability to perform well over a variety of operating conditions ranging from idling to takeoff and cruising [8]. The increase in cross-sectional area serves to reduce the coolant jet's momentum as it is turned parallel to the surface by the mainstream. Figure 1.5 illustrates the effect of the hole expansion in the leading edge region of a model turbine blade for two hole designs with the same mass flow rate. Clearly, the jet from the cylindrical hole is not attached to the surface and as a result, warmer gas is brought to the surface of the airfoil.

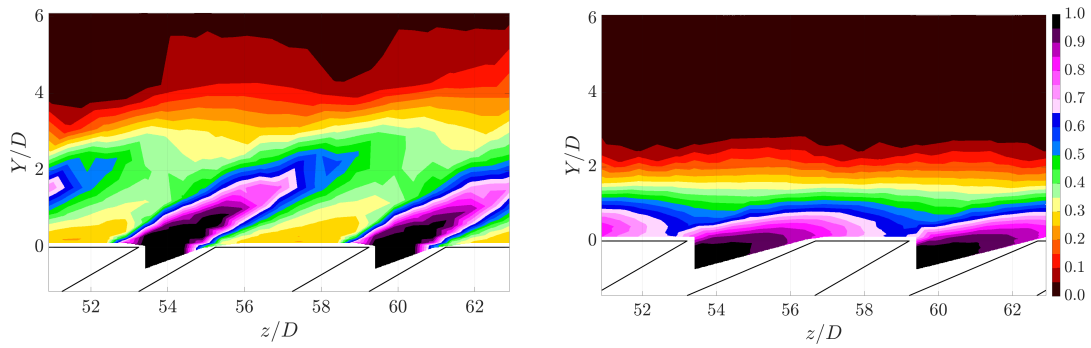

(a) Cylindrical Hole (b) Shaped Hole

Figure 1.5: Comparison of leading edge cylindrical vs shaped hole nondimensional temperature profile at blowing ratio $M = 3.10$.

For the common laidback fan-shaped hole shown in Figure 1.6, the hole features a cylindrical cross-section at the inlet, known as the metering hole with length L_m. There is a forward expansion angle β_{fwd} as well as a lateral expansion angle β_{lat}. The

forward expansion serves to reduce the angle that the coolant must turn as it exits the hole while the lateral expansion increases the jet area that the mainstream sees and allows it to turn more efficiently towards the wall [11]. As the hole-to-hole pitch P decreases, the coolant jets may merge, which is advantageous for reducing hot spots in between the jets. However, the airfoil is under an immense mechanical load and structural considerations prevent the use of the ideal case as P trends to zero: a slot that spans with height of the airfoil and dispenses a uniform blanket of coolant.

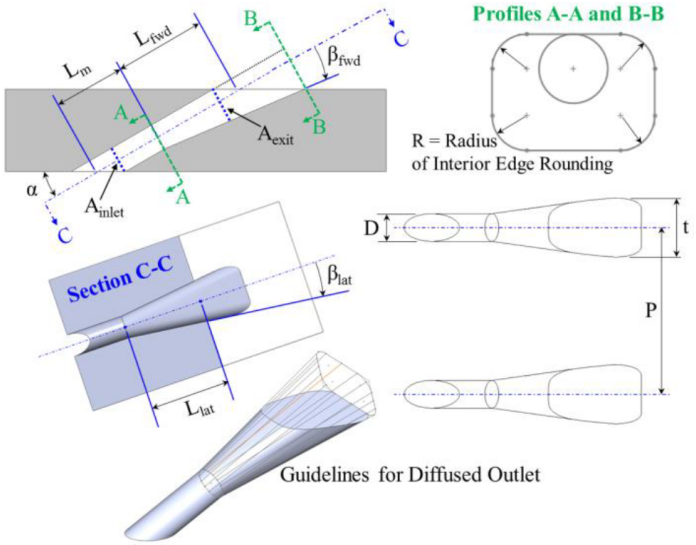

Figure 1.6: Geometric parameters for Schroeder and Thole's baseline laidback fan-shaped hole, adapted from [13].

As many film cooling hole designs are proprietary and may be subject to export control restrictions, the performance of actual film cooling holes is not widely available in the public literature. In 2014, Schroeder and Thole proposed a baseline shaped hole that is representative of hole designs used in engines in order to provide a benchmark to compare new designs against. The hole, denoted "7-7-7" features a

metering hole with length $L_m = 2.5$D, and 7° forward and lateral expansion angles. A study by Jones [14, 15] found that a 15° lateral expansion angle with a 1° forward expansion was the optimal configuration for conventional laidback fan-shaped holes fed from a channel with strong internal crossflow.

1.3.3 Relevant Nondimensional Parameters and Performance Metrics

A series of nondimensional parameters allows for comparison of film cooling operating conditions between laboratory settings and engine scales. The Reynolds number, which falls out of the Navier-Stokes equation as a similarity parameter along with the Mach number, compares the relative contribution of inertial and viscous forces and is defined using the hole diameter as a length scale and the fluid properties of the mainstream:

$$Re_D = \frac{\rho_\infty U_\infty D}{\mu_\infty} \tag{1.13}$$

The film cooling hole operating conditions are often characterized by the density ratio DR, velocity ratio VR, and their products.

The density ratio relates the coolant density to that of the mainstream flow and is a function of the relative pressures and temperatures via the ideal gas law:

$$DR = \frac{\rho_c}{\rho_\infty} \tag{1.14}$$

The velocity ratio is calculated using the average velocity in the metering hole section of the film cooling hole as the following:

$$VR = \frac{U_c}{U_\infty} \tag{1.15}$$

The maximum velocity in the hole may far exceed the average velocity due to the presence of a separation region near the sharp inlet of conventionally manufactured holes. Note that this is not the same as the channel velocity ratio VR_c that applies to film cooling designs fed by an internal channel in a co-flow, counter-flow or cross-flow configuration as defined in Equation 1.16. The internal channel velocity U_i is defined as the average velocity at the inlet of the channel, and is expected to change after mass is removed via the film cooling holes.

$$VR_c = \frac{U_i}{U_\infty} \tag{1.16}$$

The blowing ratio is the most common operating metric in the literature and compares the mass flux ratio of the coolant to the mainstream:

$$M = \frac{\rho_c U_c}{\rho_\infty U_\infty} \tag{1.17}$$

The momentum flux ratio has been shown to be a strong predictor of jet separation and is defined as [11]:

$$I = \frac{\rho_c U_c^2}{\rho_\infty U_\infty^2} \tag{1.18}$$

In evaluating integrated cooling designs, the extraction ratio r_x is important as it relates the rate of mass removal via the film cooling holes $\dot{m}_c$ to the total mass entering the channel $\dot{m}_{c,in}$:

$$r_x = \frac{\dot{m}_c}{\dot{m}_{c,in}} \tag{1.19}$$

As laboratory conditions are hundreds, if not thousands, of degrees cooler than engine temperatures and can be geometrically scaled, it is important to match the

thermal resistance through the solid with the heat load that the component sees. This is accomplished by matching the Biot number Bi to engine conditions:

$$Bi = \frac{h_\infty t}{k_m} \tag{1.20}$$

In Equation 1.20, the convective heat transfer coefficient conventionally refers to the external flow, although it can also be defined with respect to internal conditions as long as the definition is consistent between lab and engine conditions. The solid conductivity k_m and the thickness t refer to the airfoil wall. If the Biot number and the ratio of external to internal heat transfer coefficients h_∞/h_i are properly matched, the nondimensional temperature profile through the solid will be matched as well. As wall thicknesses and external heat transfer coefficients vary depending on location on the airfoil, the Biot number ranges from 0.4 to 1.6 [16].

1.3.4 Additive Manufacturing Considerations

Similar to internal cooling geometries, additive manufacturing enables complex film cooling designs not possible with conventional subtractive manufacturing techniques. Recently, Jones [14, 15] showed that the addition of a 0.25D radius fillet at the inlet of a film cooling hole improved adiabatic effectiveness over a wide range of operating conditions for a $7-7-7$ hole fed by cross-flow. This was accomplished by reducing the separation bubble that forms at the inlet of the film cooling hole as the flow turns to enter the bore of the hole.

Roughness is an additional concern for additively manufactured film cooling holes. Stimpson et al. [17] showed that the AM build process significantly distorted

the internal geometry of the hole and reduced flow for a given pressure ratio compared to smooth holes produced with conventional electrical discharge machining (EDM). Figure 1.7 shows a comparison of the resulting holes, with the center EDM hole performing better due to increased film effectiveness [17].

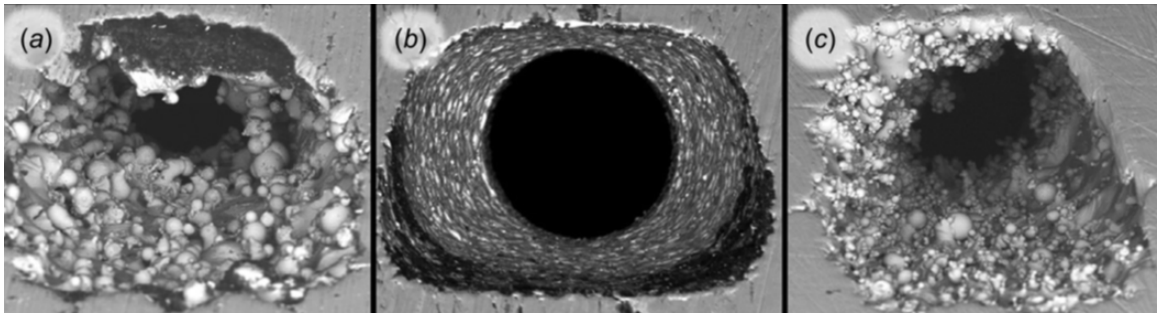

Figure 1.7: Micrographs of film cooling hole surface finish for a) $0.381mm$ hole produced with AM, b) $0.381mm$ hole produced with EDM, and c) $0.762mm$ hole produced with AM. Adapted from [17].

1.4 Thermal Barrier Coatings

Thermal barrier coatings (TBC) have been an ubiquitous part of gas turbine designs since the 1960s [18]. A ceramic layer with a high maximum temperature tolerance and low thermal conductivity is applied to the exterior surface of the airfoil in order to reduce its maximum temperature exposure and prolong its lifespan. Historically, yttria-stabilized zirconia has been the most common material used as a TBC.

TBC designs consist of a metallic bond coat approximately half the thickness of the TBC layer that provides oxidation resistance and bonds the ceramic layer to the metal alloy blade [18]. A range of typical TBC parameters is given in Table 1.1. The

exterior TBC layer is deposited on top of the bond coat and can range in thickness depending on the application. This process can introduce surface roughness which may enhance heat transfer to the surface as well as interfere with the film cooling hole design by blocking off a portion of the hole exit [8].

Table 1.1: Table of typical geometric and thermal parameters for TBC coatings.

Parameter	Value
TBC Thermal Conductivity	0.1 W/m-K [8, 19]
TBC Thickness Range	0.1-0.7 mm [19]
Airfoil Thermal Conductivity	1.0 W/m-K [19]
Airfoil Thickness Range	1.5-3.0 mm [12]

Thermal barrier coatings are known to spall with thermal cycling and historically have been considered unreliable [18]. Thus, cooling circuits have been designed such that the internal and film cooling are capable of protecting the blade even in the case of TBC failure by spallation. As material science advances enable more reliable TBCs, turbine cooling designs will incorporate TBC as an essential component rather than as an add-on to existing film-cooled configurations.

1.5 Integrated Cooling Designs

Studies of thermal designs incorporating TBC are limited in the open literature. There are at least 5000 publications of film cooling performance to date and many have studied the performance of film cooling alone and integrated film and internal cooling designs [8]. However, the optimal cooling configuration for the internal and film designs changes with the addition of TBC as the relative importance

of each cooling mode changes and the TBC layer's insulating effects dominate over film cooling [19]. In addition, simplified 1D models of integrated designs often fail to accurately predict the metal surface temperature due to the effects of lateral conduction between film cooling jets. In order to capture the combined effects of the TBC, film, and internal cooling, a matched-Biot number model must be used.

One of the first studies of the combined effects of TBC and film cooling was a computational investigation by Na et al. [20] that analyzed cylindrical holes in a flat plate fed by a co-flow channel. Na et al. found that the addition of a TBC increased overall effectiveness by as much as 30% while reducing lateral conduction between film cooling jets and led to stronger spanwise temperature gradients. Maikell et al. [21] evaluated the effect of a TBC layer on a simulated leading edge with three rows of showerhead cooling holes. The results showed that models with a TBC had an increased area-averaged ϕ of $\Delta\bar{\bar{\phi}} = 0.15$ on the simulated TBC-metal interface and a reduced sensitivity to angle of attack compared to the case without a TBC.

Davidson et al. [22] analyzed the effect of adding a TBC layer to a full vane model with a three-pass serpentine channel internal cooling design. Without film cooling, the addition of a TBC increased ϕ by 200% from 0.1 to 0.3 and provided and provided an insensitivity to mainstream turbulence intensities from 0.5% to 20%. When film cooling holes were added, the overall effectiveness increased by as much as 0.3 and and showed consistency across blowing ratios as the insulating effect of TBC compensated for the negative effects of jet separation at higher blowing ratios [22].

Davidson et al. [23] analyzed round holes, trenches, and craters with a TBC and found that although these more complex film cooling geometries provide bet-

ter effectiveness on the external surface, the TBC-metal interface temperature was relatively unchanged. The authors noted that these designs may be useful where the maximum TBC temperature is a concern, but are more difficult to manufacture conventionally and may lead to premature TBC spallation.

Stewart et al. [19] showed that even a TBC layer that was 35% less thermally resistant than that used by Davidson et al. [23] still provided an insulation effect that reduced the sensitivity of overall effectiveness to film cooling blowing ratio. This study held internal cooling effects constant and did not account for the decrease in effectiveness as coolant is extracted via film cooling. Their results showed that the effect of bore cooling through the hole is enhanced with a TBC and suggests that the optimum thermal configuration with a TBC will be significantly different than that without a TBC. This study seeks to bridge the gap between the previous studies of TBC effects and those that evaluate combined film and internal geometries.

1.6 Objectives of Current Study

With the exception of the computational study by Na et al. [20], all previous studies to date have investigated TBC effects on vane models or those with high curvature such as the leading edge region. The effects of internal cooling configuration with both TBC and film cooling has not been explored and is the focus of this study. First, a literature review was conducted to identify commonly used cooling designs for HGP turbine components. From there, computational models were used to identify trends in overall system design with variable film cooling designs and operating conditions, and a variety of internal cooling configurations that are known to be used

in industry. The computational setup is described in Chapter Two. It is important to note that the results from the computational models are not expected to align perfectly with the experiments as Reynolds-Averaged Navier-Stokes (RANS) models are known to under-predict turbulent mixing for film cooling. Rather, the models are used to identify promising cooling configurations to evaluate experimentally and allow for insight such as the flow features in the film cooling holes and the full temperature distribution at the TBC-metal interface. The top-performing designs were chosen to be evaluated experimentally.

A new test plate was designed for the recirculating wind tunnel facility at the University of Texas Turbulence and Turbine Cooling Research Lab (TTCRL), and the experimental procedures will be outlined in Chapter Three. Steady-state experiments were conducted to evaluate the contributions of individual cooling modes to overall effectiveness and quantify the effects of operating conditions such as velocity ratio and channel velocity ratio. The optimum velocity ratio for a system with film cooling was found to change with the addition of enhanced internal cooling and an applied TBC. The results will be presented and compared to the computational analysis in Chapter Four. Finally, key findings and recommendations for future work will be summarized in Chapter Five.

Chapter 2

Computational Methods

The computational fluid dynamic (CFD) analysis for this project used ANSYS Fluent to perform a Reynolds-Averaged Navier-Stokes simulation. A description of the computational domain is presented along with the boundary conditions and meshing methods. The realizable $k-\epsilon$ model is discussed along with the convergence criteria. A grid-independence study was performed to assess the discretization error and the results are presented.

2.1 Geometric Description

The computational domain for this analysis consisted of a coolant channel beneath a solid layer through which the film cooling hole was installed as shown in Figure 2.1. The coolant flow is aligned with the mainstream above the solid, and flows from left to right. The channel height of $H = 3.4$D was chosen to match the channel dimensions to engine-scale coupons manufactured by collaborators at Penn State University.

A laidback fan-shaped $15-15-1$ hole with an inlet fillet of 0.25D was tested. The intersection of the downstream edge of the diffuser outlet with the top surface of the simulated metal was taken to be the $x = 0$ position. The channel extended 20D

upstream of the hole and 60D downstream. The mainstream extended 15D above the external surface.

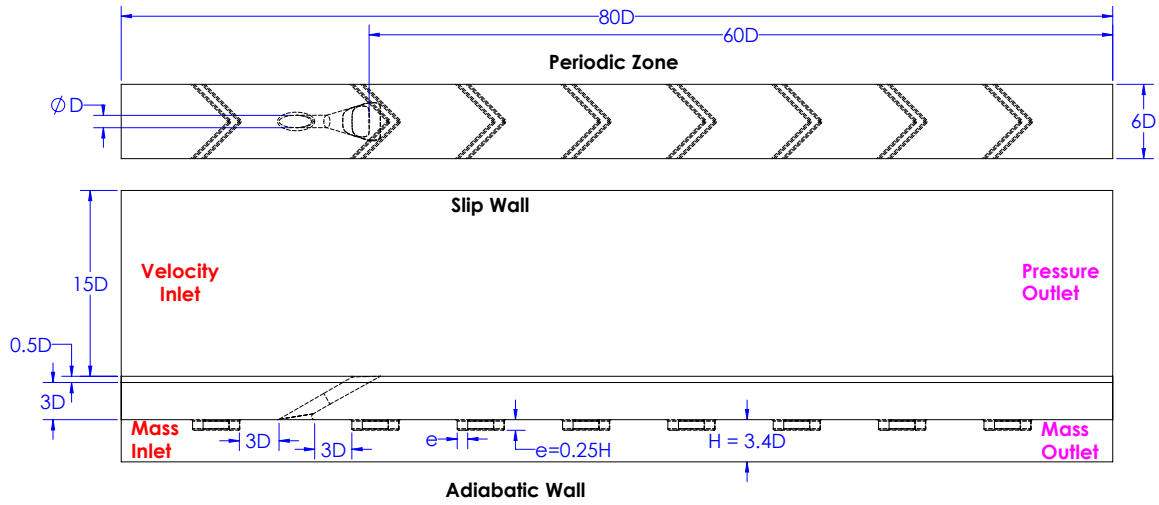

Figure 2.1: Dimensions of computational domain used for RANS analysis in ANSYS Fluent, normalized by film cooling hole diameter.

Configurations with a smooth channel as well as rib-turbulated channels were investigated. The choice of rib design was motivated by a desire to use ribs as a means of simulating the heat transfer and friction factor augmentation from the AM process. Studies of turbulator configurations in square channels by Han et al. [24] showed that 45° V-shaped ribs provide a Nusselt number enhancement Nu/Nu_0 of approximately 3x and a friction factor enhancement of f/f_0 of approximately 10x for the range of internal channel Reynolds numbers to be used in this testing, which is similar to that reported by Stimpson et al. [10] for engine-scale channels produced with direct metal laser sintering (DMLS).

2.2 Boundary Conditions

In order to reduce computational time and simplify the analysis, only one film cooling hole pitch was simulated. Linear periodic conditions at the $z = 3D$ and $z = -3D$ planes simulated a row of film cooling holes similar to engine and test conditions. For the coolant channel, a mass flow rate and static temperature of 245.8K were specified at the inlet to achieve a density ratio of 1.2. The inlet turbulence intensity Tu was set to 0.5%. Turbulence intensity is a ratio of the rms fluctuating velocity component $u = U - \bar{U}$ to the average velocity $\bar{U}$ as follows:

$$Tu = \frac{u}{\bar{U}} \tag{2.1}$$

The mass flow rate through the film cooling hole was set by adjusting the mass flow rate at the outlet of the coolant channel. The mainstream utilized a velocity inlet condition with a uniform profile and $Tu = 5\%$ in order to match the experimental conditions from Jones [14]. The temperature was set at 295K in order to match that of the laboratory conditions. A pressure condition was imposed at the mainstream outlet. All walls, with the exception of the top of the mainstream, utilized enhanced wall functions coupled with a refined mesh near the surface to resolve important near-wall features. At the y-limits, the solid boundaries were specified as adiabatic, along with the coolant channel floor. The details of the inflation layer generation will be discussed in the following section. The top of the mainstream utilized a slip condition so that the computational domain did not need to extend more than 15D above the surface, where there is little impact on the cooling performance.

2.2.1 Material Properties

For both the coolant and mainstream flows, air was modeled as an ideal gas using the three-coefficient Sutherland model for the temperature dependence of viscosity [25]:

$$\mu = \mu_0 \Big(\frac{T}{T_0}\Big)^{1.5} \Big(\frac{T_0 + S}{T + S}\Big) \tag{2.2}$$

In this equation, μ_0 is the viscosity at reference temperature T_0 corresponding to $\mu_0 = 1.716x10^{-}5$ kg/m-s and $T_0 = 273.1$K. S is the Sutherland constant of $S = 110.6$K. Kinetic theory was used to model the thermal conductivity of air. The thermal conductivity of the solid was set to match the materials used in the laboratory with $k_{TBC} = 0.065$ W/m-K and $k_{metal} = 1.02$ W/m-K.

2.3 Turbulence Model and Convergence Criteria

The Realizeable $k-\epsilon$ (RKE) turbulence model [26] was chosen for this analysis after a previous study by Jones et al [27] found that it predicted coolant velocity and distribution at the hole exit better than the $k-\omega$ and SST $k-\omega$ models. The changes to the RKE model compared to the standard $k-\epsilon$ model allow for better accuracy in regions of strong velocity gradients or separation [27].

A coupled pressure-velocity solver was used with a least-squares cell-based gradient scheme for spatial discretization. The coupled solver enhances the stability of the solution but requires more than double the memory [27]. Pressure, momentum, turbulent kinetic energy, turbulent dissipation rate, and energy were all solved using a second-order discretization scheme. Residuals were converged for all cases to 10^{-6}

and quantities of interest were monitored to ensure that the solution was not changing significantly between successive iterations.

Enhanced wall functions with curvature correction were used to model fluid-wall interactions. To ensure the validity of the results, the mean velocity profile output was compared to that of a turbulent boundary layer for a case without film cooling. The velocity profile was sampled at three locations on the TBC surface at $X/D = 20, 40, 60$, and the nondimensionalized results are presented in Figure 2.2.

For a turbulent boundary layer, the distance from the wall y and the mean velocity u can be normalized by a friction velocity u_τ as follows, where ν is the kinematic viscosity:

$$u^+ = \frac{u}{u_\tau} \tag{2.3}$$

$$y^+ = \frac{y u_\tau}{\nu} \tag{2.4}$$

The friction velocity is a function of the wall shear stress as follows:

$$u_\tau = \sqrt{\frac{\tau_w}{\rho}} \tag{2.5}$$

In the range of $30 \leq y^+ \leq 90$, the normalized velocity profile adheres closely to the logarithmic relation defined below:

$$u^+ = \frac{1}{\kappa} + log(y^+) + B \tag{2.6}$$

In Equation 2.6, the constants have been empirically determined to be $\kappa = 0.41$ and $B = 5.2$. The use of this method to nondimensionalize the velocity profile causes the curves from different locations to collapse for comparison.

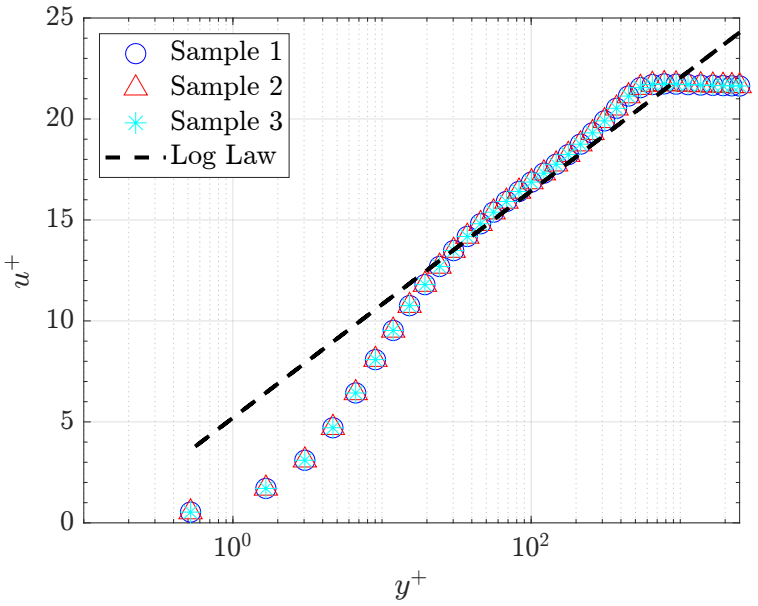

Figure 2.2: Comparison of CFD mean velocity profiles in boundary layer with expected log law profile.

2.4 Grid Generation and Independence

2.4.1 Description of Meshing Methods

The computational domains were created in the computer-aided design (CAD) tool Solidworks 2019 before being transferred to ANSYS Workbench Version 2020 R2. A boolean operation in Design Modeler was used to subtract the solid body (metal and TBC regions) from the fluid region in order to obtain a contact surface between the fluid and solid. Next, the geometry was transferred to the Meshing tool in ANSYS Workbench to convert the domain into a discretized grid.

An unstructured tetrahedral mesh was used for this analysis. The curvature capture feature was enabled in order to resolve the highly curved film cooling hole geometry. The shared topology feature was also used in order to enforce consistent

sizing across fluid-solid and solid-solid interfaces. A symmetry condition at the maximum and minimum $z-$planes enabled the periodic condition used in Fluent. Settings were adjusted such that the TBC region had at least three cells across the layer.

2.4.2 Mesh Sizing and Grid Independence Analysis

A grid independence study was performed to determine the appropriate mesh sizing with the goal of reducing the error introduced into the solution by the process of breaking a continuous domain into discrete elements. For this analysis, the quantity of interest (QoI) is the spatially-averaged overall effectiveness ($\bar{\phi}$) on the metal-TBC interface. A Richardson Extrapolation method was used to estimate the exact quantity and the error at varying grid resolutions via the following model [28]:

$$q_h - q_{exact} = Ch^p \tag{2.7}$$

In Equation 2.7, h is the resolution parameter corresponding to the grid spacing. The quantity q_h is the QoI at resolution level h, and q_{exact} is the limit of the QoI as h tends to zero. The constant C and convergence rate p are independent of h. For a second order discretization scheme, p is expected to be approximately two. Solving the model at three different grid resolutions $h_{0,1,2}$ and rearranging terms gives the following equations for q_{exact} and p:

$$q_{exact} = \frac{q_2 q_0 - q_1^2}{q_0 + q_2 - 2q_1} \tag{2.8}$$

$$p = \frac{log\left(\frac{q_2 - q_{exact}}{q_1 - q_{exact}}\right)}{log(r)} \tag{2.9}$$

A uniform refinement simplifies the analysis by allowing the introduction of the parameter r:

$$r = h_2/h_1 = h_1/h_0 \tag{2.10}$$

As an example, the grid independence study for the geometry with a smooth internal channel and a $15 - 15 - 1$ shaped film cooling hole used five grids, each with a uniform refinement $r = 1.22$. Five grids were used as the first two were found to be not within the asymptotic region where this analysis is valid. Grid resolution was set by systematically reducing all sizing controls used in the mesh generation, including the resolution of the curvature capture feature. The inflation layer height was held fixed such that the it covered the entire expected boundary layer thickness and the first cell off the wall had height $y^+ \leq 1$. Figure 2.3 shows $\bar{\bar{\phi}}$ for each mesh used, while Figure 2.4 shows the laterally-averaged effectiveness.

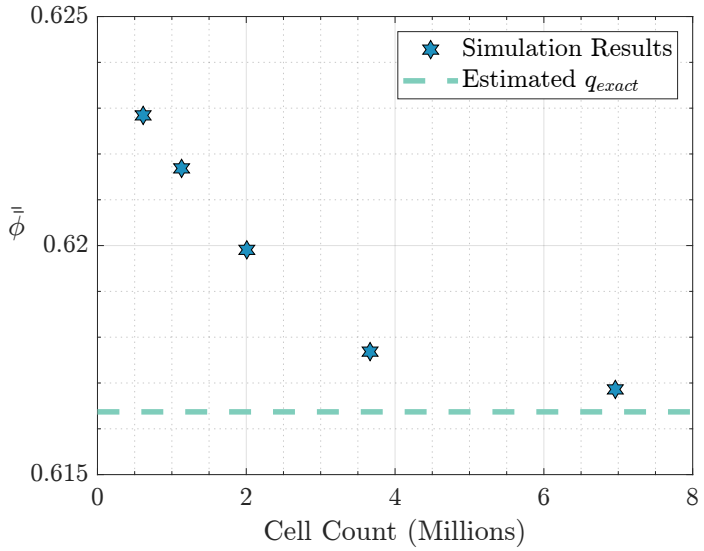

Figure 2.3: Quantitative results of grid independence analysis

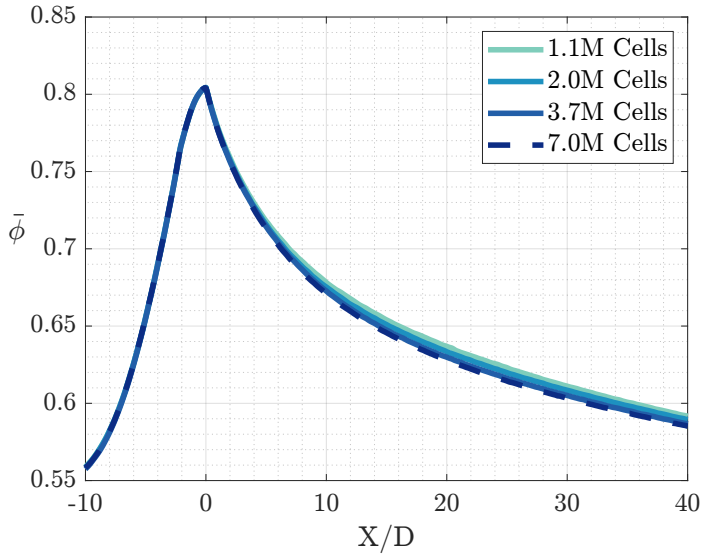

Figure 2.4: Laterally-averaged effectiveness on TBC surface for multiple grid resolutions.

The resulting convergence rate $p = 2.02$ agrees with expectations for a second-order scheme. The grid sizing controls corresponding to the mesh with 3.66 million cells was chosen for future analysis as its error of 0.21% was deemed acceptable and provided a reasonable computational time. The maximum mesh size in the domain was limited to 0.25D.

Although the average metal-TBC interface temperature does not change significantly between the various meshes used, Figure 2.5 shows that the flow field changes qualitatively between the various meshes. The forked jet behavior develops as the cell count increases and the solver is able to resolve finer flow features.

The computational results will be presented and compared to experimental results in Chapter Four.

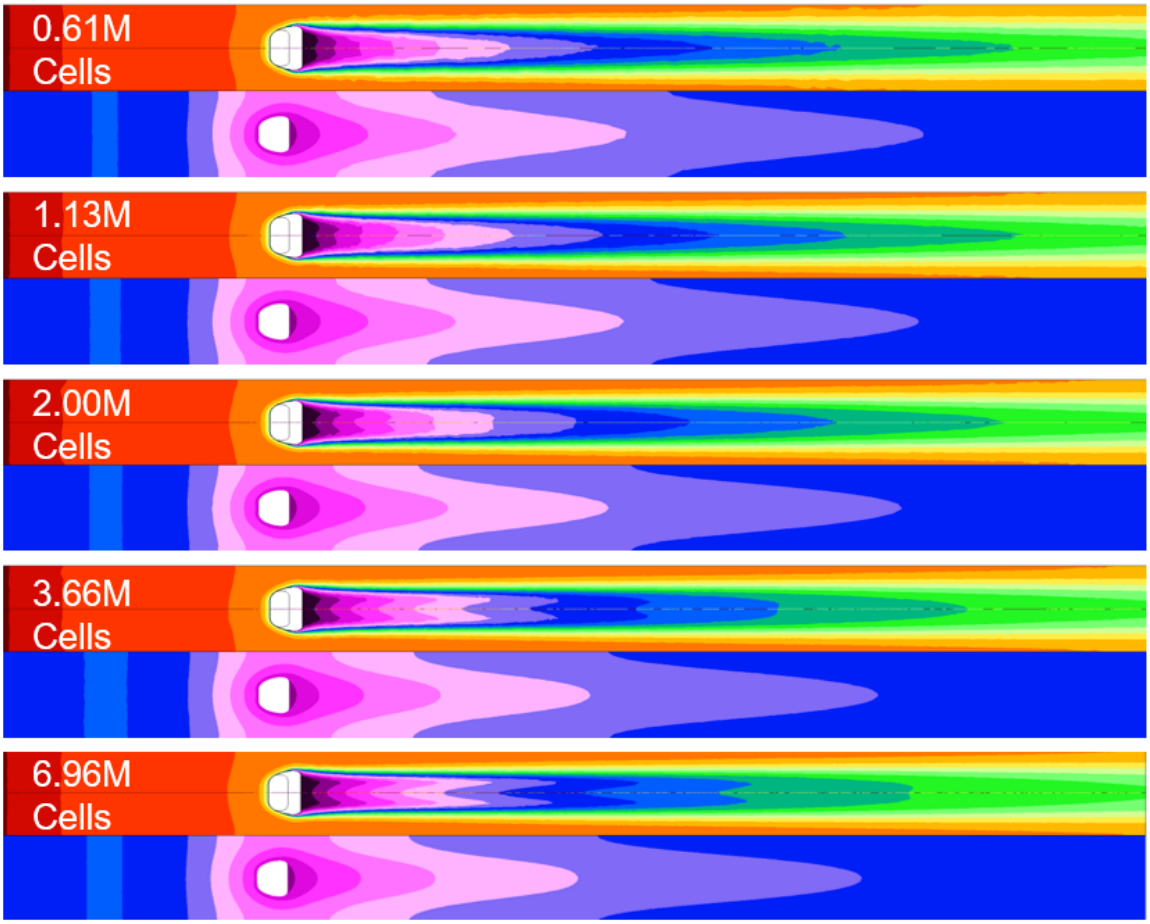

Figure 2.5: Qualitative results of grid independence study. Top contour shows top surface of TBC. Bottom contour is metal-TBC interface.

Chapter 3

Test Facility and Experimental Methods

Experiments were conducted in the closed-loop low-speed flat plate wind tunnel facility in the Turbulence and Turbine Cooling Research Laboratory (TTCRL) at the University of Texas at Austin. This section gives an overview of the various flow loops and describes the design of a new test section built for the present study.

3.1 Overview of Wind Tunnel System

The facility used for this experiment is a recirculating wind tunnel constructed by Engineering Laboratory Design in 1989 shown in Figure 3.1. The mainstream flow loop operates at atmospheric pressure, with the temperature maintained by a closed-loop control system. A cryogenic cooling system provides chilled air to the film cooling holes in order to provide a density ratio between 1.0-2.0. The test section is 6 inches high by 24 inches wide and is fed by a 9:1 contraction in order to provide a uniform velocity profile. The maximum velocity in the test section $U_\infty = 70$ m/s, corresponding to a Mach number $M_\infty = 0.2$.

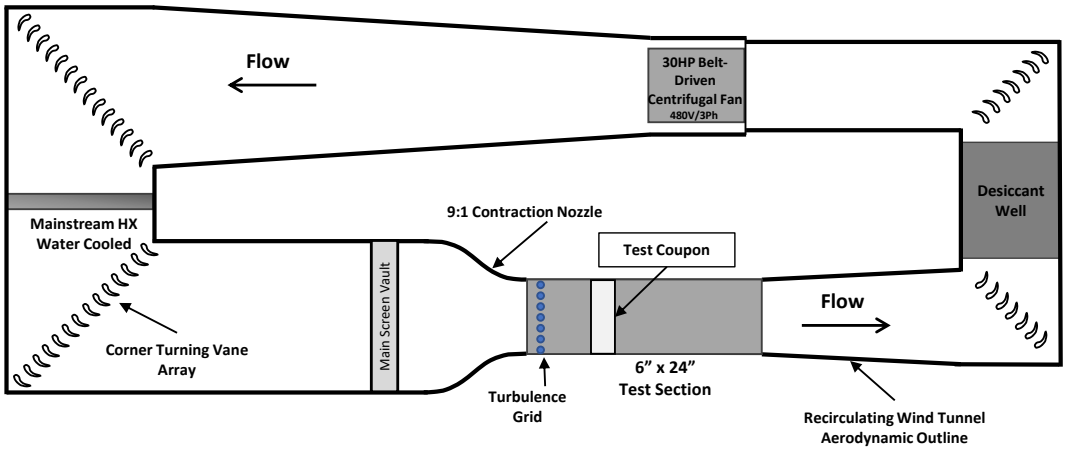

Figure 3.1: Diagram of wind tunnel facility used for the present study. Adapted from [29].

3.1.1 Mainstream Flow Conditions

The mainstream flow is powered by a 30 HP belt-driven centrifugal fan. Aerodynamic turning vanes provide smooth flow conditions around each of the four corners. Upstream of the test section, honeycomb screens condition the flow before it enters the contraction nozzle. A turbulence grid with variable diameter bars allows for control of the test section turbulence intensity between $0.2 - 18\%$.

For this study, the mainstream flow temperature was maintained at 295K by an Omega CN8262 PID controller with feedback from a Type-E gas thermocouple in the test section. The controller commands a three-way valve that can provide chilled or heated water to a two-pass heat exchanger coil located in the wind tunnel as shown in Figure 3.2. Chilled water is provided to the loop from the facility supply, and a 60 gallon tank provides thermal stability to the system.

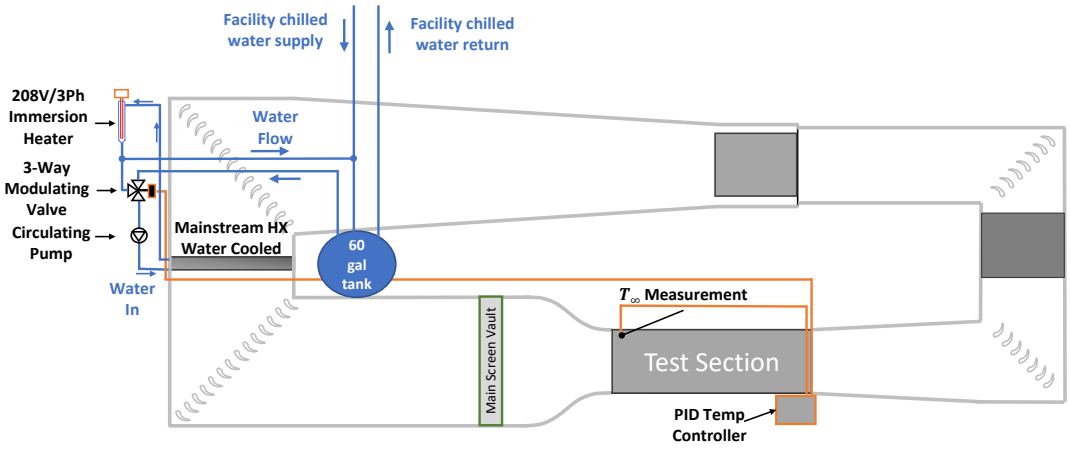

Figure 3.2: Diagram of wind tunnel mainstream temperature control system and feedback loop. Adapted from [29].

The secondary flow loop shown in Figure 3.3 serves two purposes: a low pressure blower provides suction to remove the aerodynamic boundary layer upstream of the test section and a high pressure blower provides air at cryogenic temperatures as the coolant for the film cooling holes. The boundary layer is allowed to redevelop such that the thickness can be controlled at the film cooling hole location using a trip wire.

Downstream of the low pressure blower is a steel drum containing sheets of desiccant to reduce the relative humidity of the flow and prevent frost in the coolant lines. For these experiments, three desiccant sheets were placed in the drum and two were placed in the desiccant well in the mainstream loop, typically leading to relative humidity values of 1.5% at steady-state operation. The desiccant sheets were dried after each experiment in an oven at 505K.

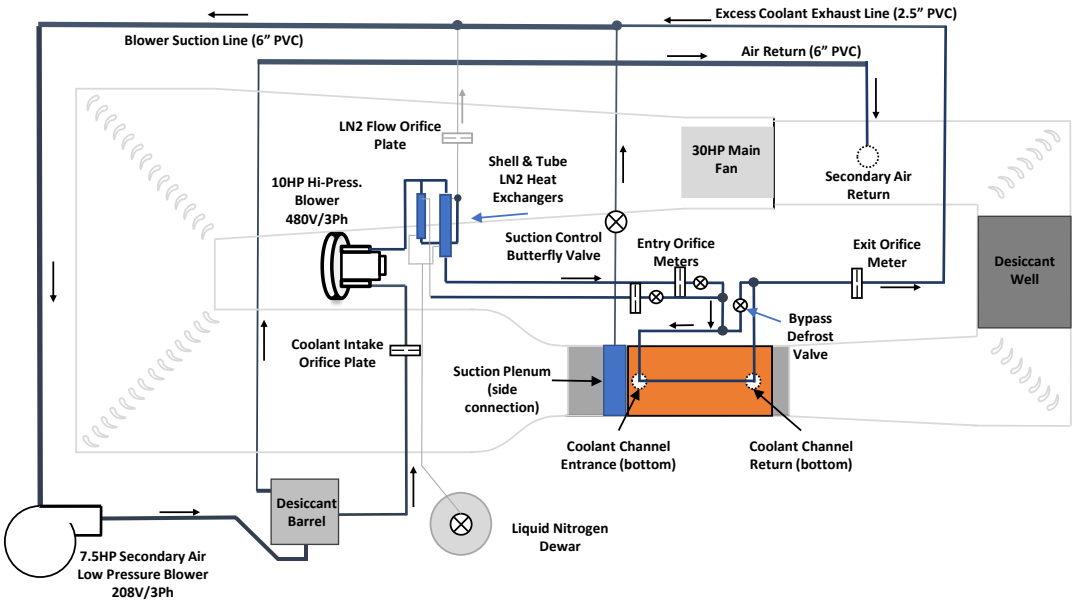

Figure 3.3: Diagram of wind tunnel secondary flow loop and coolant supply system. Adapted from [29].

A 10 HP high pressure regenerative blower connected to a variable frequency drive (VFD) downstream of the desiccant drum drives coolant through two heat exchangers supplied with liquid nitrogen from a dewar. The temperature of the coolant is controlled by adjusting the flow rate of liquid nitrogen to the system via a hand valve on the dewar. An orifice meter after the heat exchanger measures the coolant mass flow rate to the test section, which can be adjusted via a globe valve downstream of the orifice and by adjusting the blower power via the VFD. The flow rate through the film cooling holes can be adjusted via a second globe valve downstream of the test section. A Venturi meter measures the flow rate downstream of the test section, and the difference between the upstream and downstream flow

rates is the mass exiting the film cooling holes. The test section contains ten film cooling holes in order to maximize the difference in flow rates at a given operating condition to reduce the percent uncertainty. During operation, the channel velocity ratio VR_c and the hole velocity ratio VR are monitored in real-time as well as the Reynolds number through the downstream Venturi meter to ensure that it was within its calibrated range.

3.2 Design of New Test Section

The test section used for this experiment was designed specifically for this experimental campaign. Care was taken to maximize the range of operating conditions possible while matching the hole Reynolds number and Biot number within the geometric constraints.

3.2.1 Design and Material Selection

The target Biot number range of 0.4-1.6 was informed by a previous study from Dees et al. [16] with input from General Electric. The wall thickness for shaped film cooling holes is nominally 3D, and the target Reynolds number of 6200 was designed to match the work of Jones [14]. These conditions are summarized in Table 3.1. A flat-plate, constant heat flux correlation [30] was used for the external Nussult Number (defined in Equation 1.6) in calculating the external heat transfer coefficient:

$$Nu_x = 0.0308 Re_x^{4/5} Pr^{1/3} \tag{3.1}$$

DuPont Corian was chosen as the simulated metal material due to its charac-

terized thermal conductivity of 1.0± 0.1 W/m-K [23]. Based on material availability, a coupon thickness of 11.4 mm was selected for this analysis, leading to a hole diameter of 3.8 mm. In order to match the Reynolds number, the required mainstream flow velocity was 24.9 m/s. This resulted in a nominal Biot number of 0.88 at 5D downstream of the hole exit, which is well within the target range.

Table 3.1: Summary of target operating conditions

Condition	Target Value
Reynolds Number Re_D	6200 [14]
Biot Number Bi	0.4-1.6 [16]
Wall thickness	3D

The measurement surface features three test articles: an upstream Corian coupon, an additively manufactured coupon containing the film cooling holes, and a longer downstream Corian coupon as shown in Figure 3.4. The Corian was sourced from a local countertop fabricator and machined on a CNC mill.

As a focus of this study is the expanded design space enabled by AM, a thermally conductive Ice9 Rigid nylon filament from TCPoly was used to print the coupon containing the film cooling holes. The coupon was printed using a Prusa i3 MK3s fused deposition modeling (FDM) printer at 100% infill and layer height of 0.2 mm in order to achieve a thermal conductivity of nominally 1 W/m-K in the direction normal to the surface [31]. In-plane conductivity is nominally 4 W/m-K, leading to enhanced bore cooling effects upstream and downstream of the hole. To prevent warping during the print process, the coupon was printed on a glass print bed prepared with an Elmer's glue stick. The coupon is fixed to the upstream and downstream

Corian pieces using nylon screws threaded into press-fit inserts in a shoulder on the Corian components. Nylon screws were chosen over metal fasteners in an attempt to maintain a uniform thermal conductivity in the direction normal to the surface. A 1.6 mm foam gasket and a liberal coating of Dow Corning High Vacuum Grease prevented leakage between the 3D-printed coupon and the Corian section.

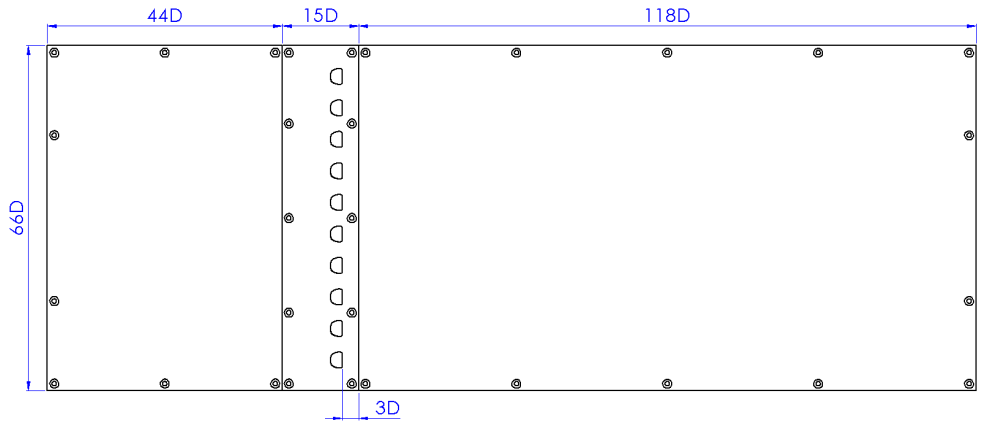

Figure 3.4: Dimensions of test articles used for this study.

Cork was chosen as the simulated TBC material in order to match the thickness and conductivity ratios with the simulated metal to engine conditions. The dimensions and conductivities are outlined in Table 3.2.

The Corian pieces and the 3D-printed coupon were attached to an acrylic housing containing the coolant channel shown in Figure 3.5 using brass screws press-fit into the acrylic. The various acrylic pieces were laser-cut by the author from 0.25" sheets at Texas Inventionworks. The acrylic sections were assembled using a methylene chloride bonding agent, then sealed with Dow Corning 737 silicone sealant.

Table 3.2: Comparison of TBC and metal parameters from engine conditions to laboratory scale.

Parameter	Engine Scale	Laboratory Scale
Airfoil Wall Thickness [mm]	2 [12]	11.4
Airfoil Conductivity [W/m-K]	20-25 [19]	1.0 [23]
TBC Thickness [mm]	0.2-0.5 [12, 18]	1.6
TBC Conductivity [W/m-K]	0.8-1.7 [19]	0.065 [22]
Thickness Ratio t_m/t_{TBC}	4.0-10.0	7.1
Conductivity Ratio k_m/k_{TBC}	12-31	15.4

The coolant was supplied via a 3" insulated PVC pipe to a custom FDM-printed transition piece that changed the cross-sectional profile from a pipe to a slot with a 12:1 aspect ratio before entering the test section. A 3:2 contraction accelerated the flow to ensure a uniform profile as it entered the test section.

The film cooling holes used for this analysis were laidback fan-shaped holes featuring a 15° lateral expansion angle and a 1° forward expansion angle. The full set of geometric parameters is given in Table 3.3.

Table 3.3: Geometric parameters for the film cooling hole used in this study.

Parameter	Value
Hole Diameter D	3.8 mm
Metering Hole Length L_m	2.5D
Injection Angle α	30°
Forward Expansion Angle β_{fwd}	1°
Lateral Expansion Angle β_{lat}	15°
Inlet Fillet Radius	0.25D
Hole-to-hole Pitch P	6D

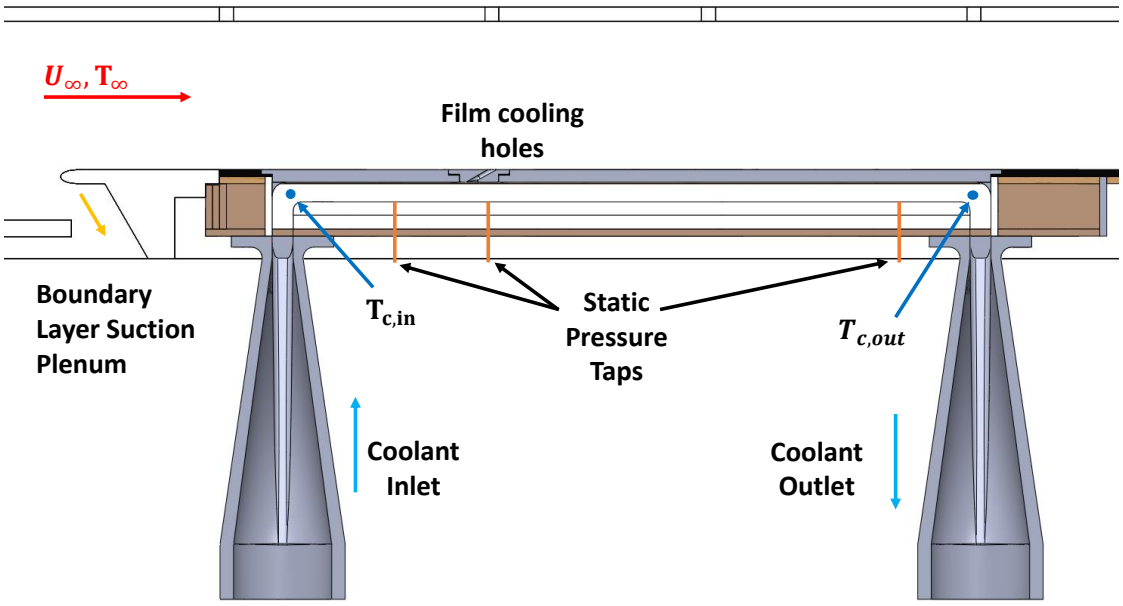

Figure 3.5: Schematic of test section and instrumentation locations

For the cases analyzed with rib turbulators in the channel, the ribs were 3D-printed using the same TCPoly filament as the film cooling coupon with $k = 1$ W/m-K normal to the surface. The ribs were adhered to the Corian sections using a 0.2 mm thick double-sided thermally-conductive fiberglass tape with $k = 1.5$ W/m-K and a minimum specified operating temperature of 243K. The tape was removed from the areas not in contact with the rib turbulators as shown in Figure 3.6. Immediately after operation, the pieces were removed from the test section to verify that the tape maintained a uniform contact area on all ribs.

Adiabatic tests were also performed to isolate the film cooling performance from the overall cooling performance. Low-conductivity foam (Last-a-Foam® R-3315)test coupons with $k = 0.043$ W/m-K replaced the Corian sections to simulate

an adiabatic surface. The coupon containing the film cooling holes was printed with a PLA filament on the same Prusa FDM printed as the matched-Biot coupons using a layer height of 0.1 mm and 10% infill, giving an effective thermal conductivity of $k \approx 0.04$ W/m-K.

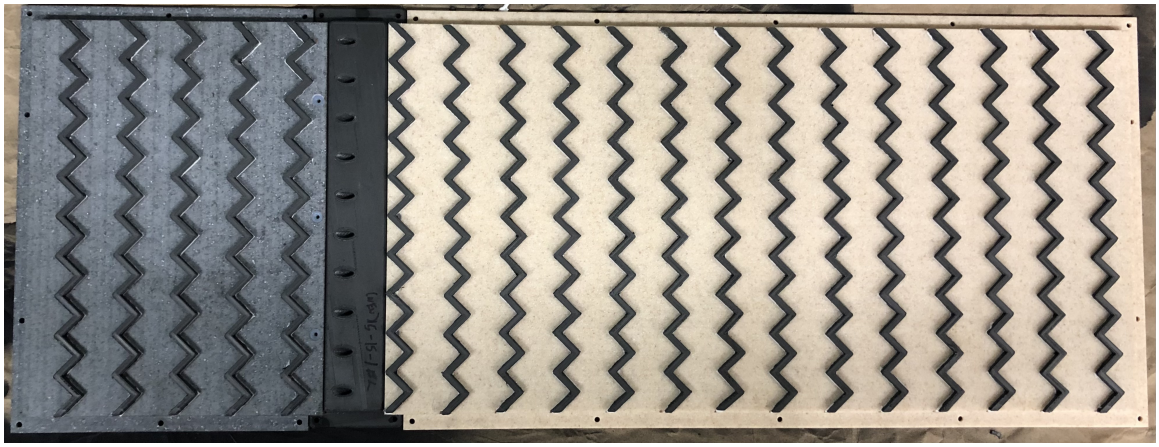

Figure 3.6: Image of rib turbulators attached to Corian test plates.

3.2.2 Instrumentation

The coolant temperature $T_{c,in}$ at the channel inlet was measured by three Type-E gas thermocouples as the coolant turned the corner to enter the channel. The temperature used in overall effectiveness ϕ calculations was an average of these three thermocouples. Two thermocouples were installed at the outlet of the channel in order to quantify the heating of the coolant over the length of the channel.

Five pressure taps were installed in the channel: one at the channel inlet, three below the film cooling hole inlets, and one at the channel outlet. The channel inlet line was connected to a $0 - 25$" H_2O Omega PX2650 differential pressure transducer

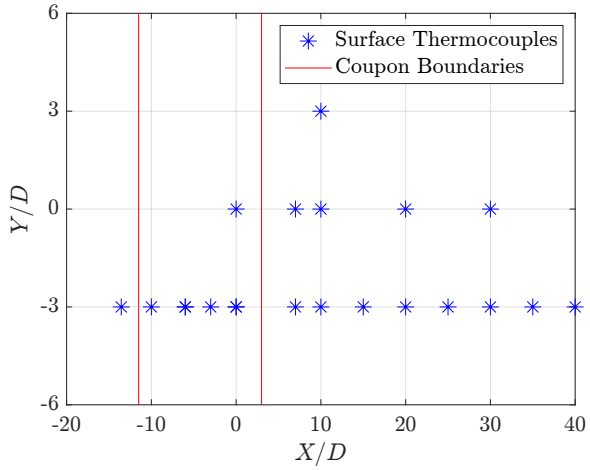

Figure 3.7: Location of thermocouples on the simulated metal-TBC interface

to measure the channel static pressure. The upstream line was also connected to a ± 2" H_2O transducer measuring the difference in channel inlet and outlet static pressures. The pressure taps beneath the holes were used in calculation of the film cooling hole discharge coefficients.

For the cases tested with a TBC, Type-E surface thermocouples were used to measure the temperature at the simulated metal-TBC interface. The location of the thermocouples, shown in Figure 3.7, was informed by the results of the CFD analysis with the goal of capturing regions of strong thermal gradients near the hole. The majority of the thermocouples were concentrated on the hole centerline, where the streamwise variation was expected to be the largest. One side of the TBC featured an adhesive layer, accounted for in the thermal conductivity measurement, that was used to bond the TBC to the Corian surface and hold the thermocouples in place.

3.3 Mainstream Flow Characterization

The suction plenum upstream of the film cooling hole location removes the boundary layer so that a new boundary layer can redevelop at the leading edge, approximately 100D upstream of the film cooling holes. This allows for control of the thickness of the boundary layer that the film cooling jets interact with. Pitot-static probes upstream and downstream of the suction plenum provide velocity measurements at each location. The volume of air removed by the plenum was set via a butterfly valve such that the upstream and downstream velocities were matched with a correction for the acceleration caused by the test section height reduction equal to half the thickness of the leading edge.

The mainstream flow turbulence intensity, length scale, and boundary layer thickness were measured using an AA-1003 hot-wire anemometer manufactured by AA Lab Systems. The probe used a 5 μm tungsten wire with an overheat ratio of 1.4 and was mounted on a Zaber T-LSR075B traverse system. Before each test, the probe was calibrated against the downstream Pitot-static probe using King's law to relate the probe output voltage V to the Pitot velocity U:

$$U = AV^4 + BV^2 + C \tag{3.2}$$

The turbulence grid used for this study had 10 mm diameter bars with 25 mm spacing. Measurements were obtained both with and without the turbulence grid installed in the tunnel with a 2 mm diameter steel trip wire placed 205 mm upstream of the film cooling hole locations. The measured boundary layer thicknesses, defined as the distance from the surface at which the local mean velocity is equal to 99%

of the freestream mean velocity, are summarized in Table 3.4. Figure 3.8 shows the profiles measured for each of the four cases. The condition with a 4.0% grid without a trip wire was chosen for the film cooling experiments as it provided a δ/D = 2.5, which is similar to the δ/D = 2.8 used by Jones [14].

Table 3.4: Summary of measured freestream turbulence intensities and boundary layer thicknesses.

Condition	Tu	Trip Wire Diameter and Location	Boundary Layer Thickness δ
A	0.2%	N/A	6.5 mm
B	0.2%	2.0 mm, 205 mm upstream	13.5 mm
C	4.0%	N/A	9.4 mm
D	4.0%	2.0 mm, 205 mm upstream	21.2 mm

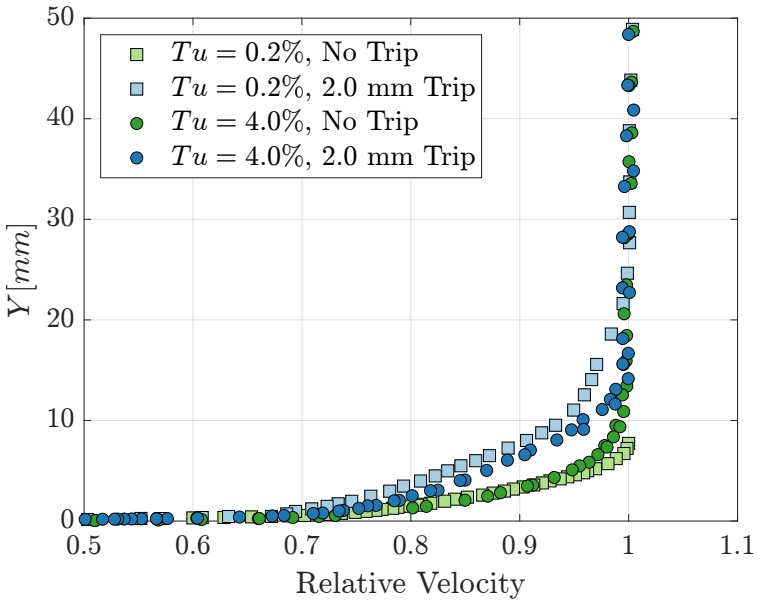

Figure 3.8: Measured velocity profiles above film cooling holes at U_∞ = 24.9 m/s

3.4 Overall Effectiveness Measurements

The overall effectiveness for each geometry tested was calculated from surface temperature measurements obtained via a FLIR A655sc infrared camera. The measurement surface was prepared using VHT Flameproof ^{TM} matte black paint to ensure a uniform surface emissivity. The measurement area consisted of four complete hole pitches in the lateral direction with the jets on either side providing periodic boundary conditions. Fiducial marks on the lateral boundaries of the measurement area enabled a spatial calibration from the raw image to a scaled coordinate system in terms of X/D and Z/D as shown in Figure 3.9.

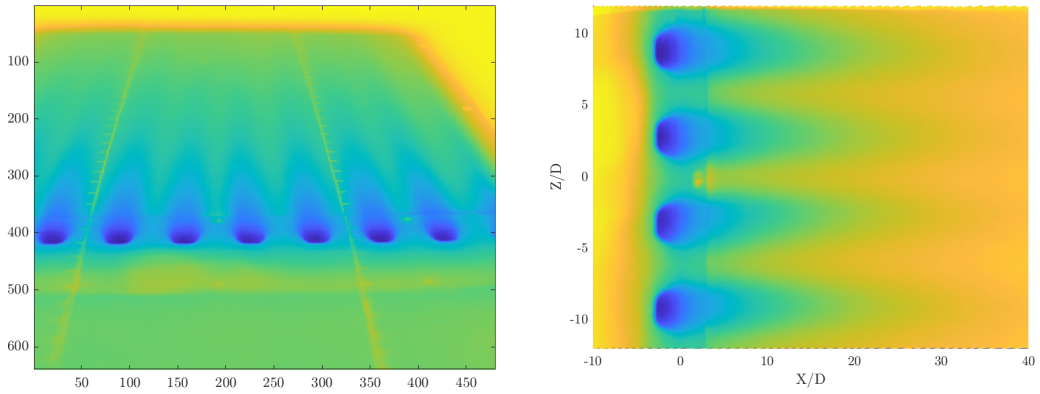

(a) Raw Image (b) Spatially-Calibrated Image

Figure 3.9: Images obtained from infrared camera before and after spatial calibration. The fiducial marks are clearly seen in (a).

The spatially-calibrated image is used in calculation of overall effectiveness ϕ at all points on the surface. An example contour map is shown in Figure 3.10.

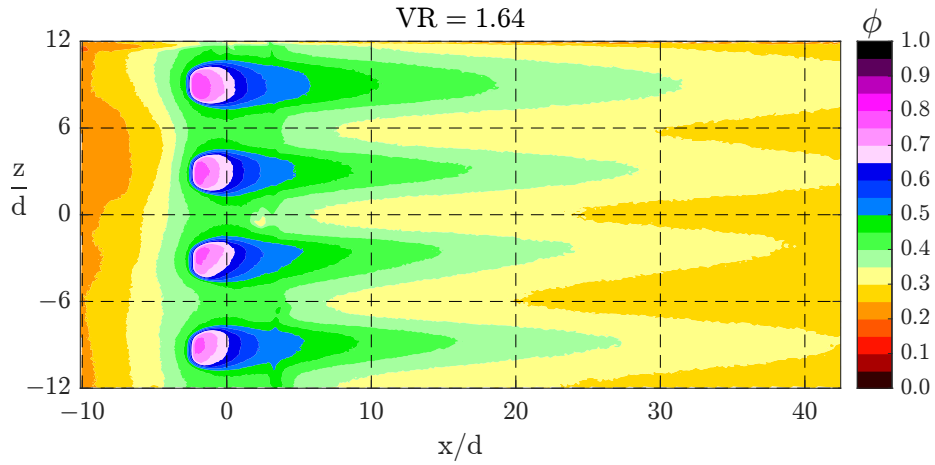

Figure 3.10: Sample contour plot of calculated overall effectiveness on external surface.

3.5 Uncertainty Analysis and Repeatability

Quantification of uncertainty is an important step in understanding the measurements obtained. All measurements have both a precision uncertainty due to random uncontrolled variation in the value and a bias uncertainty as a constant error stemming from the calibration process. Data was obtained using a National Instruments LabVIEW Virtual Instrument (VI) built by TTCRL doctoral student Dale Fox. For this analysis, five data sets of 1000 samples were obtained at 900 Hz for each measured quantity, then averaged together. The precision error $\delta_{precision}$ can be obtained by the following equation, where $S_{\bar{x}}$ is the standard deviation of the mean values of the five data sets:

$$\delta_{precision} = \pm t_{95} S_{\bar{x}} \tag{3.3}$$

The Student's t-value t_{95} is a measure of the range in which one would expect to find 95% of the values obtained [32]. The bias uncertainty is quantified via the cal-

ibration process by analyzing the variance estimate of the curve fit to the calibration data. The overall uncertainty δX for a quantity X is found via a root-sum square of the precision and bias contributions as follows:

$$\delta X = \sqrt{(\delta X)^2_{precision} + (\delta X)^2_{bias}} \tag{3.4}$$

For quantities of interest such as overall effectiveness ϕ or velocity ratio, VR, that are functions of multiple independent variables, the sequential perturbation technique outlined in Moffet [33] allows for quantification of uncertainty of the dependent variable as a function of the uncertainty of the independent variables. For a quantity R_0 that is a function of variables $x_{i=1:N}$, the uncertainty in R_0 as a function of each individual uncertainty, C_{i+}, is found by perturbing x_i by its uncertainty δx_i and calculating a new value of R with the perturbed input:

$$R_{i+} = R(x_1, x_i + \delta x_i, x_N) \tag{3.5}$$

The contribution to the uncertainty of R by the ith variable is the difference between the perturbed value R_{i+} and the original value R_0:

$$C_{i+} = R_{i+} - R_0 \tag{3.6}$$

The total uncertainty is found from a root-sum-square of the individual contributions as follows:

$$\delta R = \sqrt{\sum_{i=1}^{N} C^2_{i+}} \tag{3.7}$$

Longer-term precision uncertainty in measurements was quantified by taking in-test repeat measurement points for a single operating condition during the test and at the end of the experiment.

3.5.1 Uncertainty in Pressure Measurements

The pressure transducers used for this study were calibrated against a micro-manometer with a range of $0 - 10"H_2O$ and a larger manometer with a range of $0 - 60"H_2O$. A calibration curve was generated to convert the raw voltage output to pressure values used in future calculations as shown in Figure 3.11. It was determined that a second-order polynomial reduced the maximum bias uncertainty of the calibration.

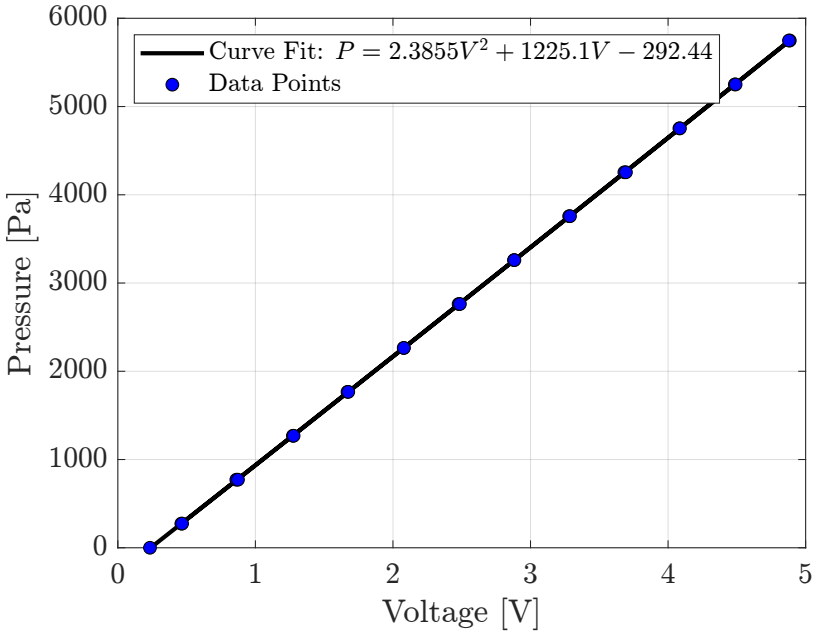

Figure 3.11: Calibration curve of $0 - 25"H_2O$ pressure transducer used to measure coolant channel static pressure.

3.5.2 Uncertainty in Velocity Measurements

Velocity in the test section was calculated via the following equation:

$$U_\infty = \sqrt{\frac{2P_{dyn}}{\rho_\infty}} \tag{3.8}$$

The dynamic pressure P_{dyn} was measured using a Pitot-static probe. The density ρ_∞ was calculated using the ideal gas law with mainstream temperature measured via an ensemble average of three Type-K thermocouples and atmospheric pressure from nearby Camp Mabry. At a mainstream velocity of $U_\infty = 24.90$ m/s, the bias uncertainty is equal to $\delta(U_\infty)_{bias} = \pm 0.01$ m/s and is dominated by the bias uncertainty of the pressure transducer. The contributions to uncertainty from the uncertainty in density are negligible. The precision uncertainty is $\delta(U_\infty)_{precision} = \pm 0.07$ m/s, leading to an overall uncertainty of $\delta U_\infty = \pm 0.07$ m/s.

3.5.3 Uncertainty in Mass Flow Rates

The coolant channel mass flow rates upstream and downstream of the film cooling holes were measured by an orifice meter and Venturi meter, respectively. The mass flow rate is calculated via the following equation:

$$\dot{m} = \rho C_d A \left(\frac{2\Delta P}{\rho(1-\beta^4)} \right)^{0.5} \tag{3.9}$$

where C_d is the discharge coefficient, A is the throat area, and β is the ratio of throat diameter to pipe diameter.

Both flow meters were calibrated before previous experimental campaigns against a laminar flow element to determine the discharge coefficient as a function

of the throat Reynolds number. The uncertainty in mass flow rate is propagated from the pressure transducer bias uncertainty as well as from the bias uncertainty stemming from the variance in the flow meter calibration curve fit. The inlet channel velocity ratio of $VR_c = 0.2000$ used for the majority of this study corresponds to a mass flow rate of $\dot{m}_{in} = 0.0201 \pm 0.0001$ kg/s measured by the upstream orifice meter. The bias uncertainty of $\delta(\dot{m}_{in})_{bias} = \pm 0.0001$ kg/s is dominated by the uncertainty from the pressure transducer calibration, while the precision uncertainty of $\delta(\dot{m}_{in})_{precision} = \pm 3x10^{-5}$ kg/s contributes negligibly to the overall uncertainty.

The internal velocity in the coolant channel U_i is a function of the coolant density and channel cross-sectional area A:

$$U_i = \frac{\dot{m}}{\rho_c A} \tag{3.10}$$

The uncertainty in mass flow rate dominates the uncertainty in channel velocity to give an overall uncertainty of $\delta U_i = \pm 0.03$ m/s at $U_i = 4.96$ m/s.

The uncertainty in channel velocity ratio VR_c (defined in Equation 1.16) is a function of the uncertainties of both the mainstream velocity and the coolant channel velocity. The bias error of $\delta(VR_c)_{bias} = \pm 0.0012$ and precision error of $\delta(VR_c)_{precision} = \pm 0.0092$ give an overall uncertainty of $\delta VR_c = \pm 0.0093$, or 4.7%.

At a film cooling hole velocity ratio of $VR = 1.67$ (defined in 1.15), the downstream mass flow rate was calculated to be $\dot{m}_{out} = 0.01824 \pm 0.00007$ kg/s, with the bias uncertainty of $\delta(\dot{m}_{out})_{bias} = \pm 6x10^{-5}$ kg/s coming largely from the pressure transducer calibration.

The mass flow rate through the film cooling holes $\dot{m}_f$ is taken to be the difference between the upstream and downstream flow meters:

$$\dot{m}_f = \dot{m}_{in} - \dot{m}_{out} \tag{3.11}$$

For the lowest velocity ratio tested, $VR = 0.414$, the mass flow rate through the film cooling holes is equal to $\dot{m}_f = (1.64 \pm 0.13)x10^{-3}$ kg/s, which is dominated by the bias error of $\delta(\dot{m}_f)_{bias} = 1.3x10^{-4}$ kg/s. This gives a relative uncertainty of $\delta(\dot{m}_f)/\dot{m}_f = \pm 7.9\%$ at the lowest velocity ratio tested. When designing the test coupon, one objective was to maximize the number of film cooling holes in order to increase the difference in measured flow rates upstream and downstream of the test section in order to reduce the relative uncertainty.

The average velocity through the metering section of the film cooling holes U_c is given as:

$$U_c = \frac{4\dot{m}}{\rho_c \pi D^2} \tag{3.12}$$

The jet velocity is used in calculation of the velocity ratio VR. For $VR = 0.414$, the bias uncertainty of $\delta(VR)_{bias} = \pm 0.033$ and precision uncertainty of $\delta(VR)_{precision} = \pm 0.018$ give an overall uncertainty of $\delta(VR) = \pm 0.038$, or $\pm 9.2\%$.

After the experiments were conducted, it was noted that the film cooling holes did not shut off as expected when the VI reported a velocity ratio of $VR = 0.00$. Due to time constraints, an analysis was performed to quantify the mass flow rate error as a function of the internal channel pressure to be applied as a correction factor to the previous measurements. The blank coupon was installed in the test section and the coolant channel flow rate was set to a channel velocity ratio of $VR_c = 0.20$ and

$VR_c = 0.10$. The upstream and downstream valves were adjusted to pressurize the channel from 100.8 to 106.1 kPa absolute and the mass flow rate difference between the upstream and downstream flow meters was recorded. The $\Delta\dot{m}$ values are shown in Figure 3.12.

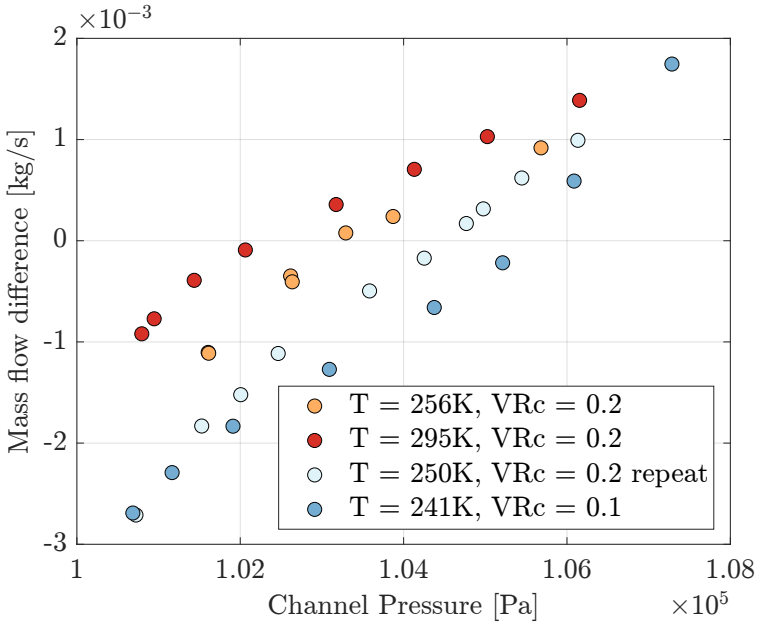

Figure 3.12: Measured mass flow rate difference as a function of coolant channel pressure.

The measured channel pressure as a function of velocity ratio is shown in Figure 3.13a. This data was used to generate a mass flow rate correction at each velocity ratio, and was applied to the measured mass flow rate shown in Figure 3.13b. The calibration, with an R^2 value of 0.99, is applied to the measured VR values as follows:

$$VR_{corrected} = 0.7744(VR_{measured}) + 0.4099 \tag{3.13}$$

The calibration adds an additional $\delta(VR) = \pm 0.10$ bias uncertainty, which domi-

nates the precision and bias uncertainties from all other sources to give an overall uncertainty of $\delta(VR) = \pm 0.11$.

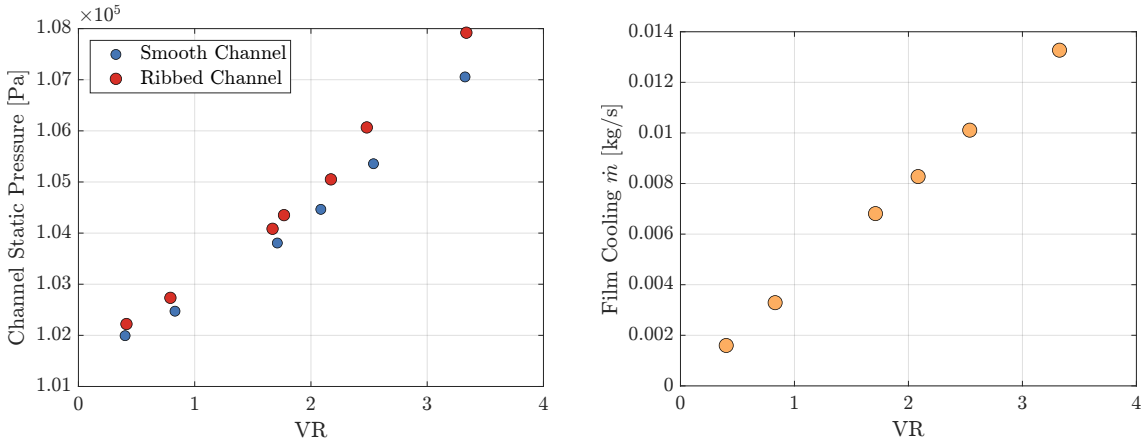

Figure 3.13: Channel pressure (a) and total mass flow rate through all film cooling holes (b) as a function of velocity ratio.

It should be noted that this is an average velocity ratio across 10 film cooling holes and does not account for non-uniform flow in the channel that may bias flow toward one hole or another, although efforts were made during the design process to maintain as uniform flow as possible.

3.5.4 Uncertainty in Temperature Measurements

Thermocouples are used for temperature measurements of the coolant and mainstream flows, surface temperature at the simulated metal-TBC interface, and as an input for calculation of gas properties at the various flow meters. The type E chromel-constantan thermocouples used for this study were calibrated in-house using a glycol bath with a high-accuracy thermistor. The bath was cooled from 300.15K

to 250.15K in 5K increments, then heated back to 300.15K. A sample calibration curve is shown in Figure 3.14. The precision uncertainty arises from the variance estimate of the calibration curve fit to the individual data points. For this particular thermocouple, the maximum precision uncertainty is $\delta T = \pm 0.05$K, which is well below the NIST uncertainty range of $\delta T = \pm 1.0$K. The bias uncertainty from the thermistor standard is negligible.

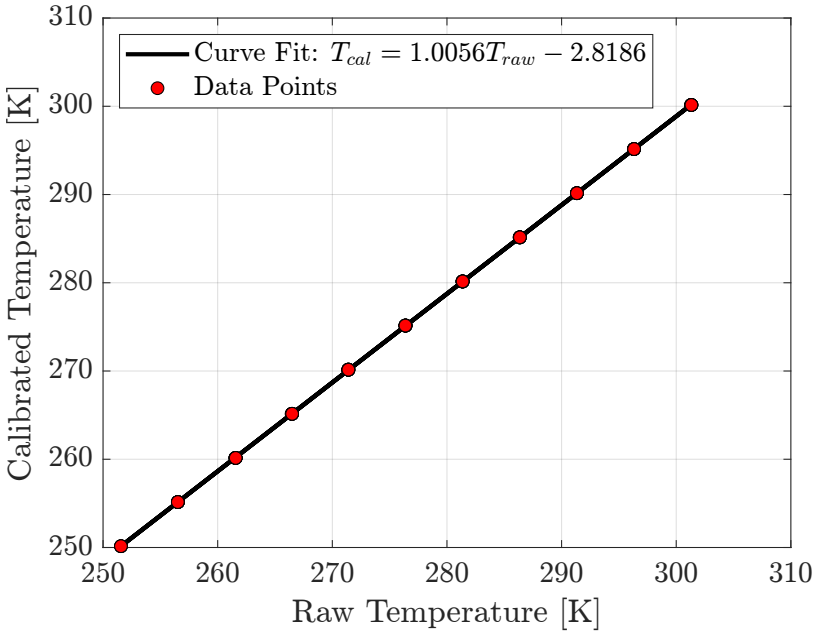

Figure 3.14: Sample calibration curve of surface thermocouple used to measure temperature at simulated metal-TBC interface.

The infrared camera used for external surface temperature measurements was calibrated in-situ against type E surface thermocouples, which were calibrated using the glycol bath discussed above. The calibration accounts for effects of the viewing angle of the camera through a zinc selenide window and emissivity of the measurement

surface. The thermocouples were adhered to a small 5x5 mm copper tab painted with the same VHT Flameproof black paint as the measurement area and placed at 10D intervals directly downstream of the film cooling holes. The copper tab provides a larger area of relatively constant temperature for the IR camera to view. The thermocouples were staggered such that the wires did not interfere with the jets interacting with downstream thermocouples. The processing code in MATLAB allows the user to select the location of each thermocouple and generates a curve fit to relate the raw IR output to a temperature measurement as shown in Figure 3.15. The precision uncertainty in the measured surface temperature stems from the process of fitting a third-order polynomial to the individual data points. Sources of bias uncertainty are the uncertainties of the individual thermocouples used as the standard as well as the selection of the thermocouple locations in the IR image.

The precision and bias uncertainties in the measured surface temperature and calculated effectiveness are a function of the uncertainties of the thermocouple and IR camera measurements. For the adiabatic effectiveness measurements, there is a bias uncertainty that comes from the conduction effects through the foam plate downstream of the film cooling holes. A future addition to the data processing procedure would be to add a correction for the conduction effects. The precision uncertainty dominates, with a maximum value of $\delta\eta_{precision} = 0.017$, coming largely from the infrared camera measurements.

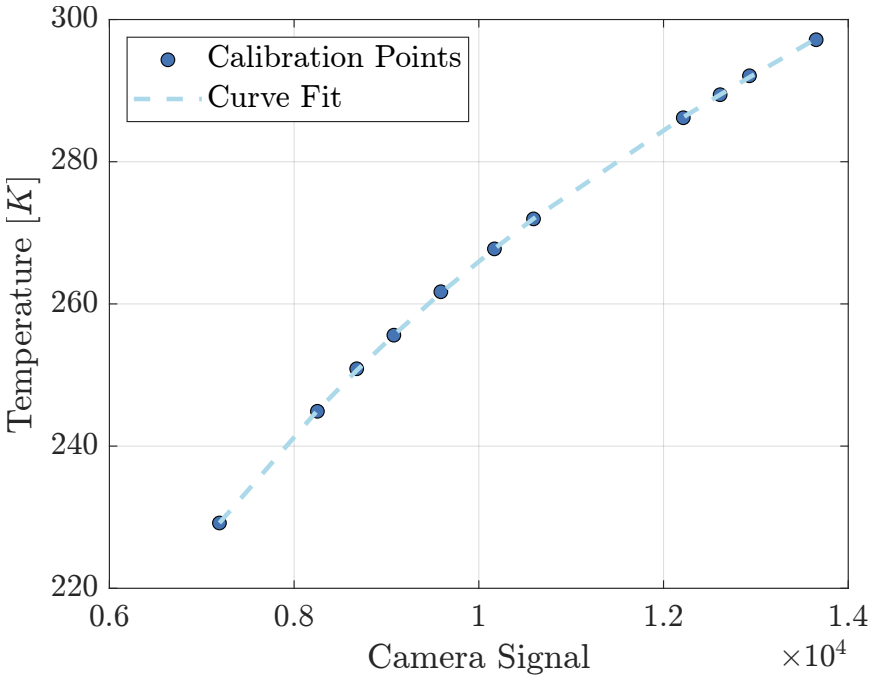

Figure 3.15: Calibration curve fit to IR calibration points with a maximum bias of 0.42 K.

3.5.5 Repeatability

At the beginning of the experimental campaign, the thermal response of the test coupons was analyzed to develop an understanding of the time required for the model to reach steady state. Once a density ratio of 1.20 was reached, measurements were taken every three minutes and processed in real-time until the laterally-averaged effectiveness on the surface did not change within uncertainty between measurements. The results are shown in Figure 3.16. For all measurements, the system was allowed to come to equilibrium for 15 minutes when moving between operating conditions, which is consistent with the technique used by Stewart et al. [19] on a Corian matched-Biot number vane model of similar thickness.

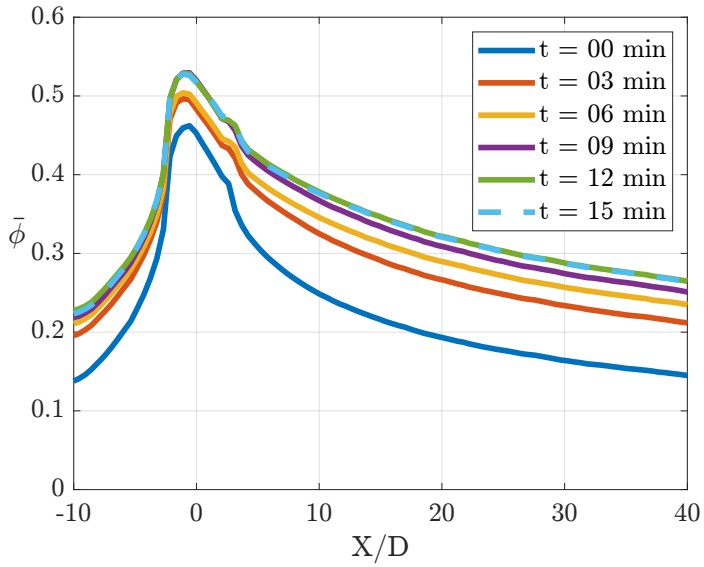

Figure 3.16: Time-dependent laterally-averaged effectiveness beginning at $t = 0$ once the target density ratio of 1.2 was obtained.

The repeatability of the measurements was verified by taking measurements at the same operating conditions at the beginning and end of the experiment as well as on different days. The test-to-test repeatability for the $15 - 15 - 1$ hole fed by a smooth channel without a TBC was tested four days later after removing and re-installing the Corian test articles and the film cooling hole coupons, and was found to be $\delta(\phi)_R = \pm 0.009$. Sample results for the repeatability tests are shown in Figure 3.17.

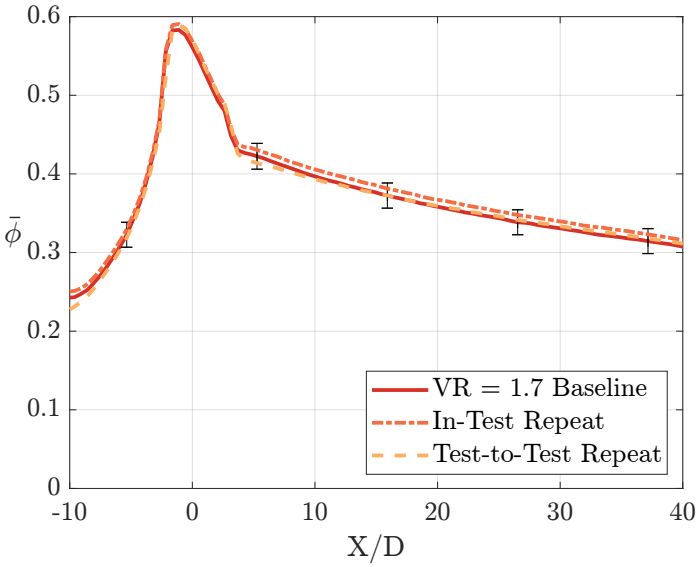

Figure 3.17: In-test and day-to-day repeatability study for the $15 - 15 - 1$ hole fed by a smooth channel without a TBC.

Chapter 4

Results

This section presents the results for isolated internal cooling and film cooling separately, as well as integrated designs, both with and without a thermal barrier coating. Computational and experimental results are compared.

4.1 Discharge Coefficients

The discharge coefficient for the film cooling holes tested was calculated using the following equation from Gritsch et al. [35] using total conditions in the coolant channel:

$$C_d = \frac{\dot{m}}{\frac{\pi d^2}{4} P_{t,c} \left(\frac{P_\infty}{P_{t,c}}\right)^{\frac{\gamma+1}{2\gamma}} \sqrt{\frac{2\gamma}{(\gamma-1)RT_{t,c}} \left(\left(\frac{P_{t,c}}{P_\infty}\right)^{\frac{\gamma-1}{\gamma}} - 1 \right)}} \tag{4.1}$$

The results as a function of the pressure ratio between the mainstream and channel are shown in Figure 4.1. The results are similar to those reported by Gritsch et al. [36] for laidback fan-shaped holes fed by a low Mach number co-flow channel, which lie between 0.7-0.8 for a mainstream Mach number of 0.0-0.3 and show increasing C_d values with increasing pressure ratio. The small discrepancy is likely due to the rounded inlet used for this study and the difference in forward and lateral expan-

sion angles. The smooth channel cases tested showed little variation in C_d with the addition of a TBC. However, the turbulated channel C_d showed an increased value with the addition of a TBC, possibly due to the increased diffuser length providing a reduction in detrimental flow features induced by the ribs.

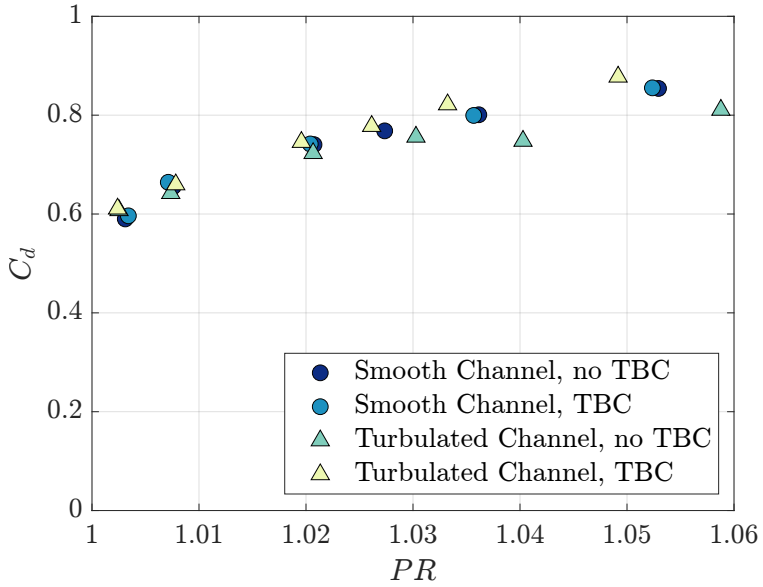

Figure 4.1: Discharge coefficients for each of the hole configurations tested fed by a co-flow channel velocity ratio of $VR_c = 0.20$.

4.2 Adiabatic Effectiveness Results

The adiabatic effectiveness results quantify the film cooling performance independent of the internal cooling. The $15 - 15 - 1$ film cooling hole (described in Table 3.3) was fed by an inlet channel velocity ratio VR_c of 0.20 over a range of velocity ratios from 0.7 to 3.0. Contours of adiabatic effectiveness η on the surface are shown in Figure 4.2 and indicate good jet uniformity in the spanwise direction.

The laterally-averaged effectiveness as a function of velocity ratio is shown in Figure 4.3. Notably, the laterally-averaged effectiveness shows a similar value downstream between $VR = 1.7$ and $VR = 2.9$, indicating that the jet does not separate at the highest velocity ratio tested, which corresponds to a blowing ratio of M = 3.5 and a momentum flux ratio of I = 10.1. This is likely due to the optimized hole geometry with the inlet fillet developed by Jones [14, 15].

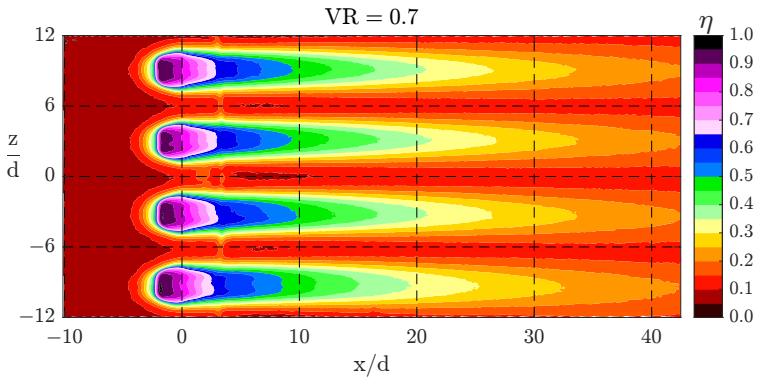

(a)

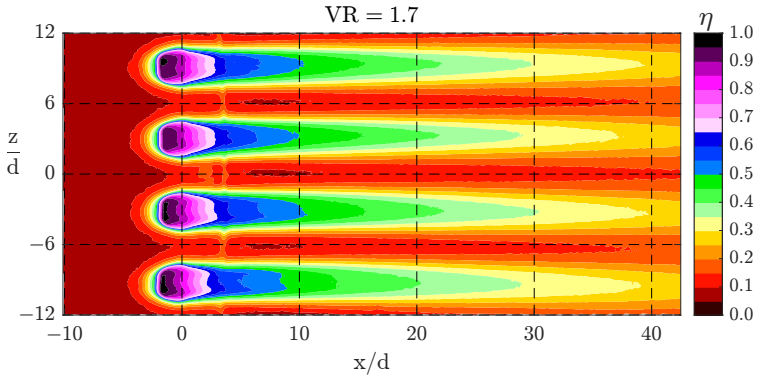

(b)

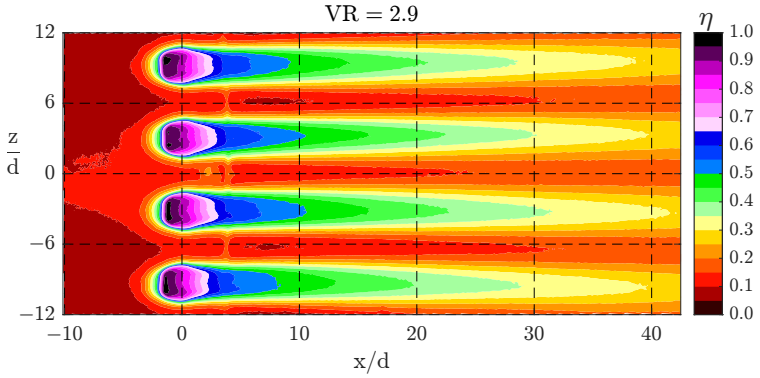

(c)

Figure 4.2: Contours of adiabatic effectiveness η for the $15 - 15 - 1$ film cooling hole fed by a co-flow channel velocity ratio of $VR_c = 0.20$.

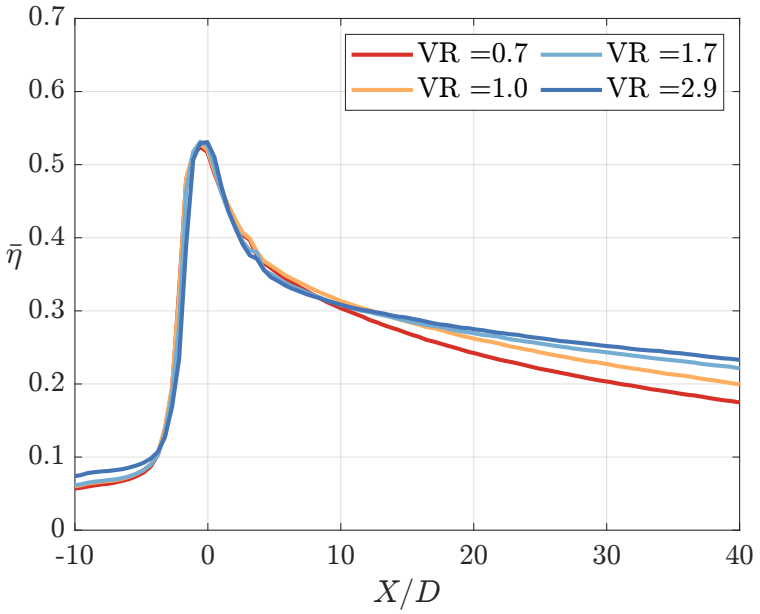

Figure 4.3: Laterally-averaged $\bar{\eta}$ for a 15-15-1 hole fed by a co-flow channel velocity ratio of $VR_c = 0.20$.

4.3 Overall Effectiveness without a TBC

4.3.1 Internal Cooling Results

The overall cooling effectiveness results, measured on the simulated metal surface, show the effect of the internal channel flow without film cooling. Figure 4.4 shows the overall effectiveness over the same region as the film cooling data, with a channel velocity ratio $VR_c = 0.1 - 0.4$, corresponding to a Reynolds number range of $5,400 - 21,700$. Using the Dean correlation for duct flow [37] valid between $6\text{x}10^3 < Re < 6\text{x}10^5$, the internal heat transfer coefficient is expected to increase by a factor of three between VR_c = 0.1-0.4. A one-dimensional heat transfer analysis

through the solid wall gives the expected effectiveness on the surface as [38]:

$$\phi = \left(1 + Bi + \frac{h_{ext}}{h_i}\right)^{-1} \tag{4.2}$$

The 1D analysis agrees with the experimental results within uncertainty for internal channel velocity ratios of VR_c = 0.2-0.4, and under-predicted the effectiveness at $VR_c = 0.1$. The discrepancy at the lowest velocity ratio is likely due to the Reynolds number being out of range of the correlation as well as additional turbulence induced by the 90° bend at the channel inlet.

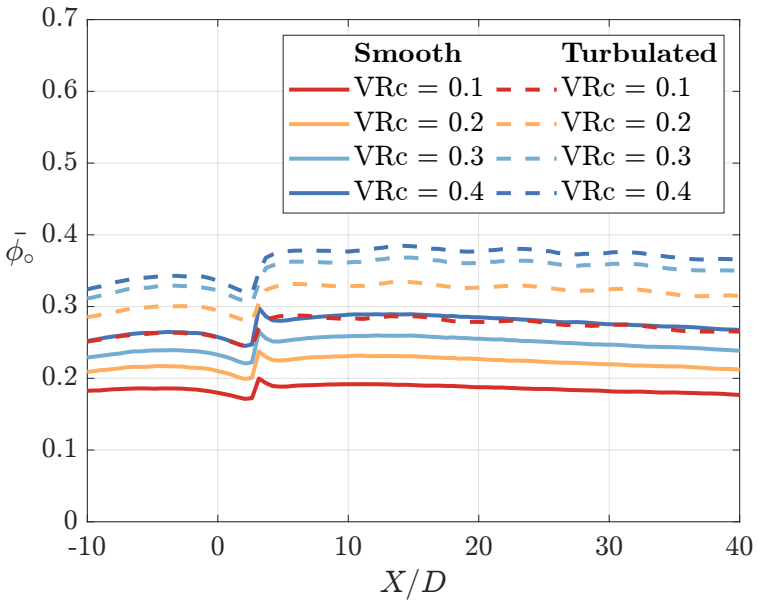

Figure 4.4: Laterally-averaged $\bar{\phi}$ at varying channel velocity ratios.

At a constant coolant mass flow rate corresponding to a channel velocity ratio of $VR_c = 0.2$, the addition of rib turbulators increased the spatially-averaged overall cooling effectiveness from $\bar{\bar{\phi}} = 0.22$ to 0.32, an increase of 44%. Notably, the turbulated channel at $VR_c = 0.1$ performs very similarly to the smooth channel with

$4x$ coolant flow. At the channel exit, approximately 120D downstream of the film cooling hole location, the smooth channel at $VR_c = 0.4$ showed a centerline temperature increase of 3.5K, compared to 12.0K for the ribbed channel, indicating a much more efficient use of coolant for the ribbed channel. The discontinuity at X/D = 3 represents the interface between the coupon containing the film cooling holes and the downstream Corian plate. The rise in effectiveness for X/D > 3 indicates that the thermal conductivity of the AM coupon is lower than that of the Corian plate in the direction normal to the surface.

While the ribbed channels showed increased effectiveness compared to the smooth channels, pressure drop is also a consideration in the design of engine components. Figure 4.5 shows the friction factor augmentation for the ribbed channel normalized by that of the smooth channel. The results are higher than the 8-9x augmentation reported by Han et al. [24] for a single pitch of the repeating rib geometry over the same Reynolds number range. The decision to use a turbulated channel would be up to the engine designer depending on the available pressure driver and heat load at each region of the airfoil.

4.3.2 Integrated Cooling Results

The addition of film cooling, shown in Figure 4.6, indicates that for velocity ratios between 1.7-3.0, the smooth channel design shows relatively constant performance. By contrast, the turbulated channel design shows a decrease in laterally-averaged overall effectiveness downstream of the film cooling holes at velocity ratios above VR = 1.7. This indicates that the coolant is used more effectively internally,

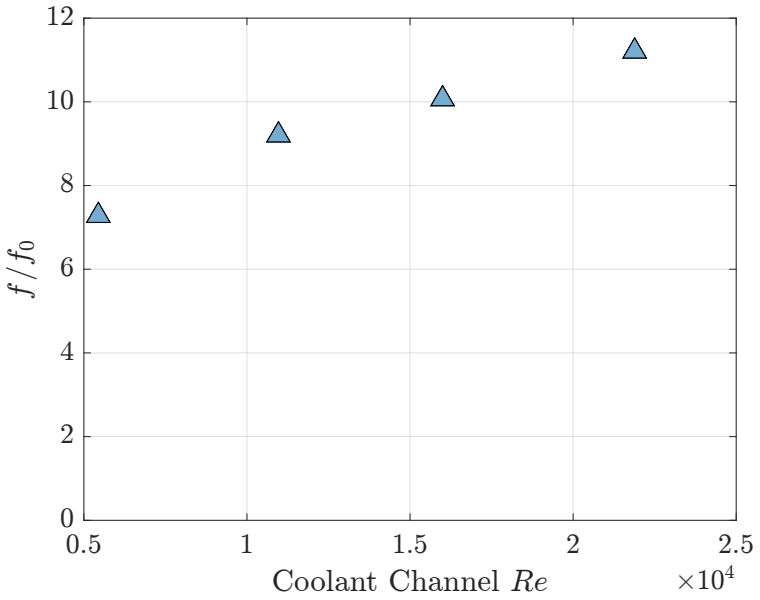

Figure 4.5: Friction factor augmentation for the ribbed channel compared to the smooth channel as a function of channel Reynolds Number.

as the heat transfer enhancement from the rib turbulators outweighs the film cooling benefit of a reduced external temperature. It is important to recognize that the channel velocity ratio is significantly lower downstream of the film cooling holes for the higher velocity ratios testing, dropping to as low as $VR_c = 0.07$ at VR = 3.0. The cases without film cooling provide a baseline for internal cooling performance with a constant coolant mass flow rate corresponding to the upstream and downstream velocity ratios. The adiabatic effectiveness results show that the jet does not separate at higher velocity ratios, indicating that the decrease in effectiveness is purely a result of reduced heat transfer in the internal channel. The sharp drop in effectiveness at X/D = 3 is again a result of the interface between the AM coupon and the Corian plate impeding the effects of bore cooling propagating downstream. This effect is seen qualitatively in Figure 4.7.

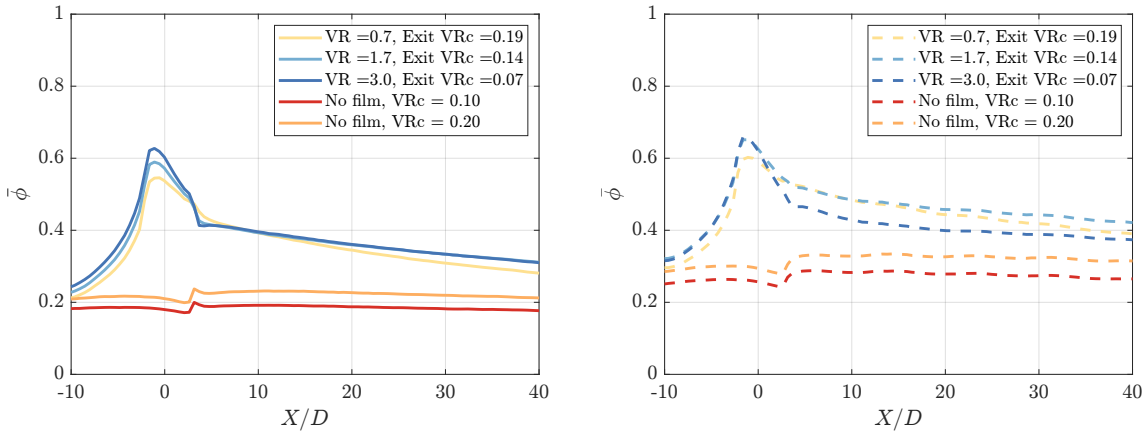

(a) Smooth Channel

(b) Turbulated Channel

Figure 4.6: Comparison of film cooling performance to baseline co-flow channel performance

At a VR = 1.7, the addition of turbulators increased the spatially-averaged effectiveness over the range 0 < X/D < 40 by 27% from $\bar{\bar{\phi}} = 0.37$ to 0.47. This effect is less pronounced at higher VR's as the turbulated channel shows an increase of only $\Delta\bar{\bar{\phi}} = 12\%$ at VR = 3.0.

Based on the CFD results shown in Figure 4.8(a) one would expect a similar drop in performance downstream for the smooth channel, although this is not seen experimentally. This is likely due to the film performance masking the effect of reduced internal cooling, which is not as significant for the smooth channel as it is for the turbulated channel.

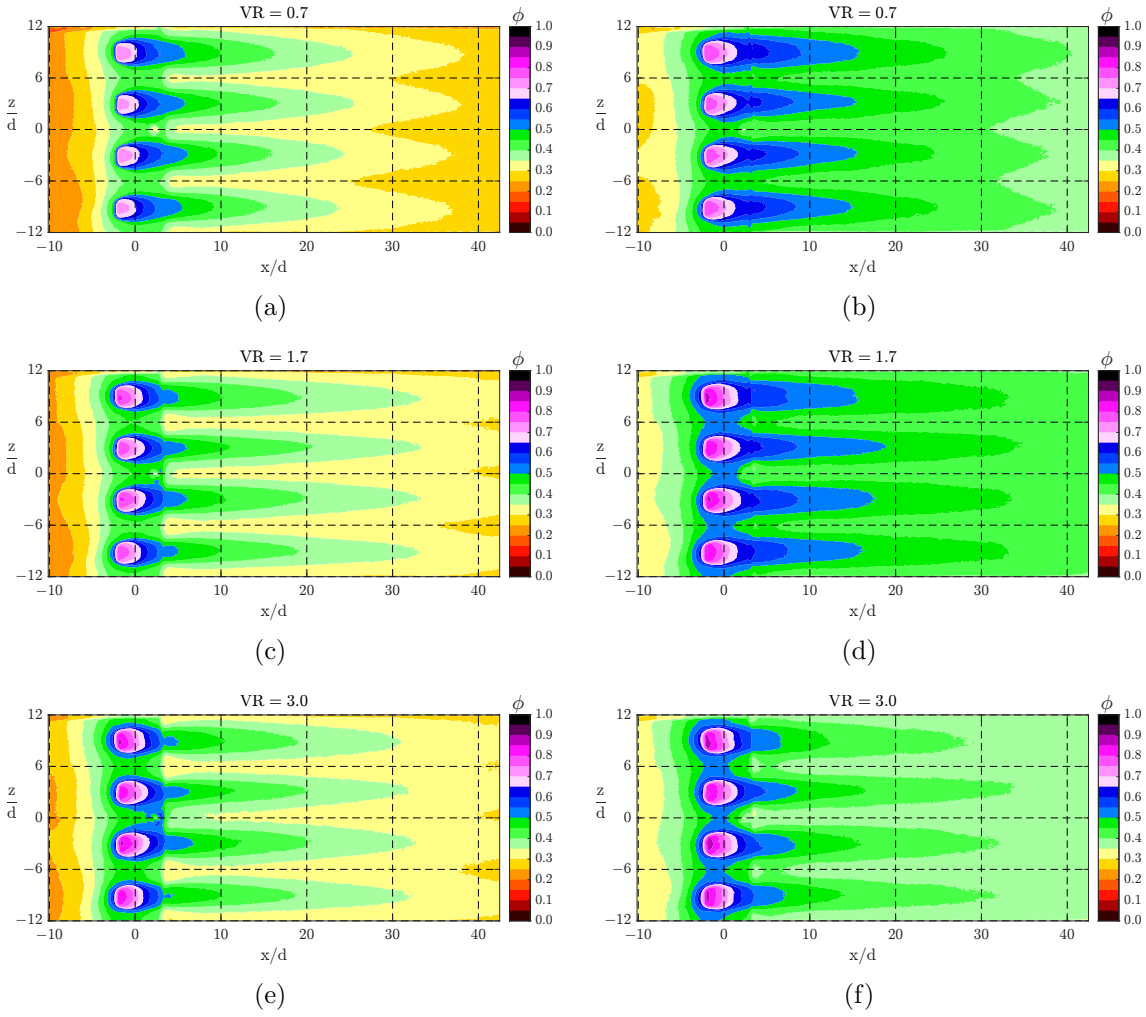

Figure 4.7: Contours of overall effectiveness ϕ for the $15-15-1$ film cooling hole fed by a smooth (left) and turbulated (right) co-flow channel velocity ratio of $VR_c = 0.20$.

4.3.3 Computational Results

The CFD analysis agrees reasonably well with the experimental results for the smooth channel. The overall effectiveness is nearly identical for both $VR = 1.67$ and $VR = 2.50$, as in the experimental data. While the computational results show a decrease in performance at a velocity ratio of $VR = 3.00$, this drop in performance was not observed experimentally. Regardless of the individual discrepancies, the CFD and experimental results all lie within the same narrow performance band, showing the strength of RANS analysis in predicting the performance of integrated film and internal cooling systems.

For the turbulated channel, shown in Figure 4.8(b), the computational results correctly predicted the trends with the $VR = 1.7$ condition performing best and showing decreased performance at $VR = 3.0$. The CFD analysis also captured the spatially oscillating thermal profile on the surface caused by the ribs at discrete locations.

The laterally-averaged effectiveness just upstream of the film cooling holes shows a higher value for the experimental data than the computational data. This can likely be explained by the enhanced bore cooling effects caused by the anisotropic thermal conductivity of the coupon containing the film cooling holes. The peak value of laterally-averaged effectiveness is lower for the computational results as the averaging process only accounted for the $y = 0$ plane, whereas the IR camera measured the solid surface just below the $y = 0$ plane at the outlet of the hole.

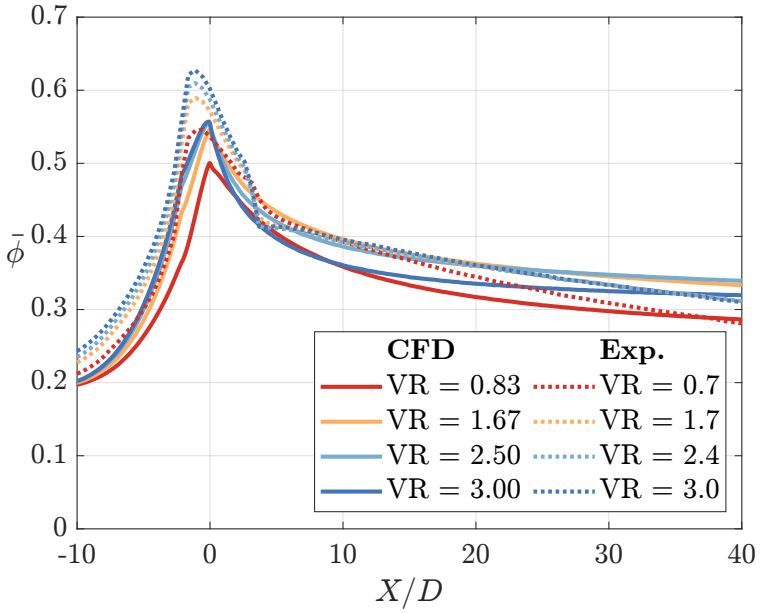

(a) Smooth Channel

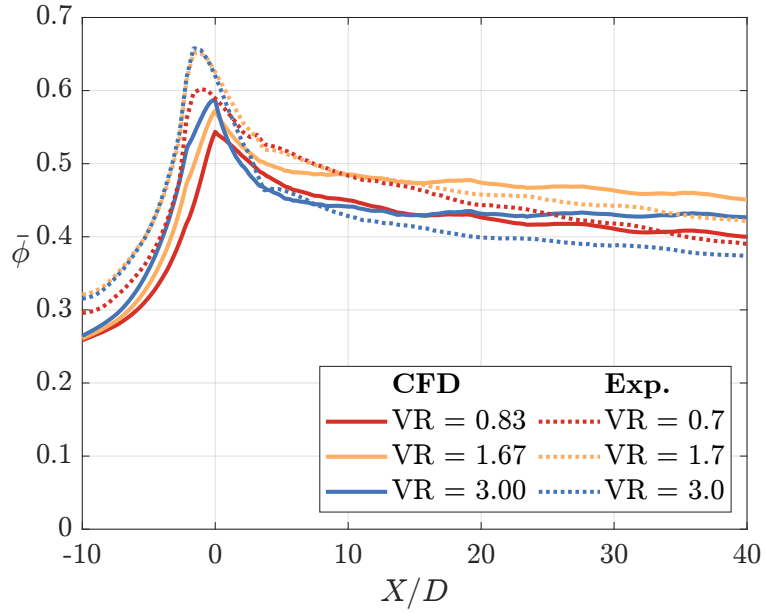

(b) Turbulated Channel

Figure 4.8: Laterally-averaged effectiveness for film cooling holes fed by a channel with inlet $VRc = 0.2$.

4.4 Thermal Barrier Coating Effects

4.4.1 Experimental Results

The cases with a thermal barrier coating were tested similarly to those lacking a TBC. Figure 4.9 shows the effectiveness on the simulated TBC-metal interface for both channel designs tested over a range of channel velocity ratios from $VR_c = 0.1 - 0.3$.

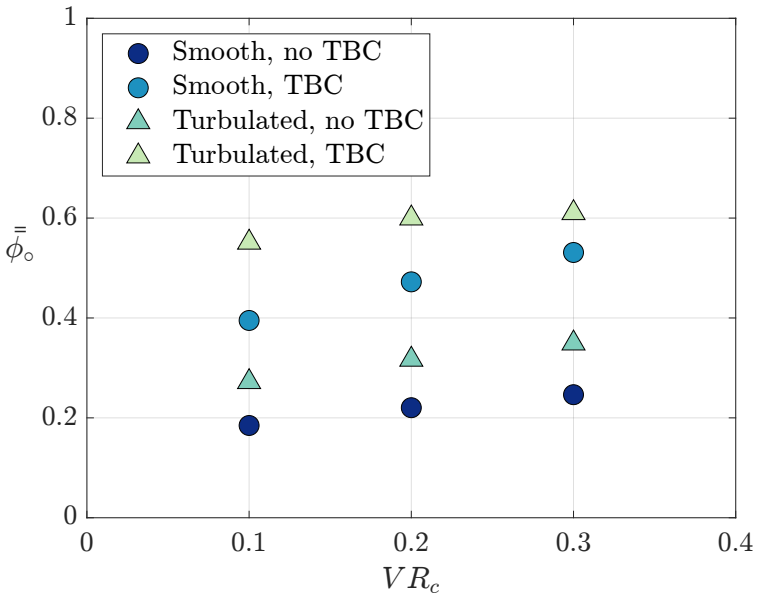

Figure 4.9: Overall cooling effectiveness on the simulated TBC-metal interface without film cooling.

The results of these experiments show that for a constant amount of coolant at a $VR_c = 0.20$, the addition of a TBC can raise the overall effectiveness by $\bar{\bar{\phi}} = 0.25$ for a smooth channel and $\bar{\bar{\phi}} = 0.28$ for the turbulated channel. The benefits of TBC and enhanced internal cooling are directly additive, with the $\Delta\bar{\bar{\phi}} = 0.10$ increase from ribs without a TBC combining with the $\Delta\bar{\bar{\phi}} = 0.28$ from the TBC giving an overall

increase in effectiveness of $\Delta\bar{\bar{\phi}} = 0.38$, or a maximum of $\bar{\bar{\phi}} = 0.60$, which was observed experimentally. This corresponds to an increase of 172% for the combined effect of TBC and ribs compared to the baseline smooth channel alloy-only case. This is an expected result as enhanced internal cooling and a thermal barrier coating operate somewhat independently of each other.

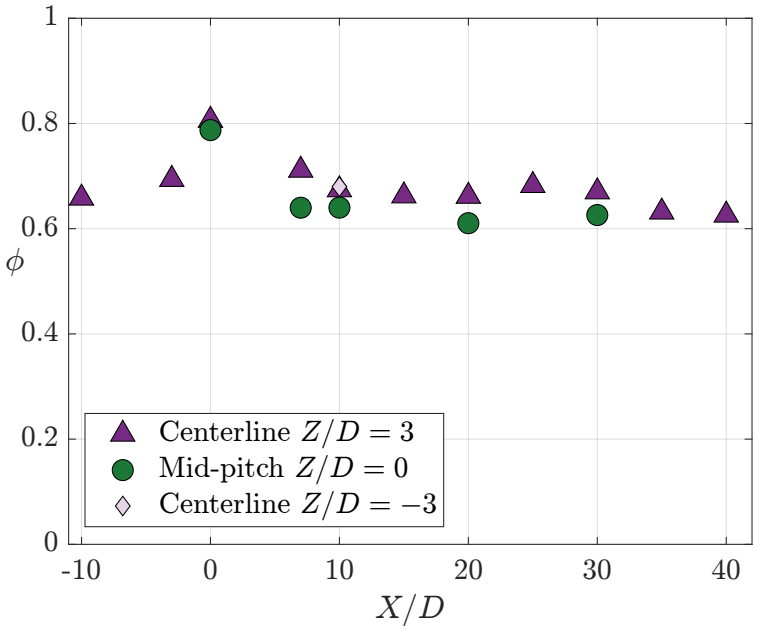

Figure 4.10: Spanwise effectiveness distribution on simulated metal-TBC interface at VR = 1.7

The effectiveness at all points measured with the addition of film cooling is shown in Fig. 4.10. As expected, the effectiveness is greatest on the hole centerline, while the mid-pitch shows slightly lower ϕ. A thermocouple on the neighboring hole pitch verified uniformity between holes at X/D = 10. The streamwise variation in effectiveness with a TBC was likely caused by the uneven external surface due to the presence of thermocouple wires beneath the TBC.

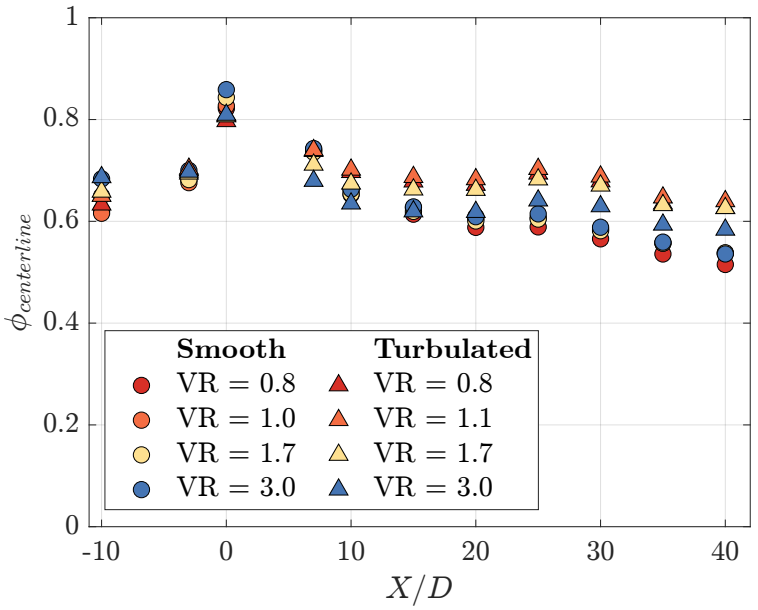

Figure 4.11: Effectiveness on the simulated TBC-metal interface for film cooling designs fed by a channel velocity ratio of $\mathrm{VR}_c = 0.2$.

When film cooling holes are added, the centerline effectiveness in Figure 4.11 shows similar values for the velocity ratios tested, a result that is consistent with the findings of Stewart et al. [19]. Notably, the smooth channel shows the highest effectiveness at a velocity ratio of $VR = 3.0$, corresponding to an extraction ratio of 0.65, while the turbulated channel drops off in performance at the same conditions. The optimum performance for the turbulated channel design is seen at $VR = 1.1$, corresponding to an extraction ratio of 0.20. This finding is significant, as it suggests that thermal designs incorporating a thermal barrier coating and enhanced internal cooling may perform better at lower velocity ratios as the coolant is more effectively used internally. However, the fact that the performance for a turbulated channel increases from VR = 0.8 to VR = 1.1 indicates that film cooling still provides a significant benefit to the overall thermal design.

The tradeoff between film cooling and internal cooling is seen again in Figure 4.12. Comparing Figures 4.12(a) and 4.12(b), one can see that film cooling provides a greater benefit to the smooth channel design than to the turbulated channel design as there is a larger difference in effectiveness. Although the effectiveness decreases at higher velocity ratios, the designs with film cooling performed better than or equal to those without film. For the turbulated channel at the highest velocity ratio tested of VR = 3.0, the designs with film cooling performed similarly to those with internal cooling alone, even though the channel velocity ratio downstream of the film cooling hole was significantly reduced. The constant adiabatic effectiveness performance between VR = 1.7-3.0 indicates that the decrease in overall effectiveness is a function of the reduced internal cooling. The effect of bore cooling is significant as well, as seen by the large increase in effectiveness near $X/D < 0$ for both channel designs. Analysis of a hole with enhanced bore cooling mechanisms would be an interesting direction for future studies.

Figure 4.13 demonstrates that the effectiveness on the external surface of the TBC is not sensitive to the internal channel conditions as both the smooth and ribbed designs show similar results. The rise in effectiveness at $X/D = 3$ is caused by a gap that formed when the cork layer on the coupon and downstream Corian components contracted, allowing coolant to spread laterally. As the film cooling holes were cut by hand from the cork sheet using a stencil, there are variations in the jet profiles in the spanwise direction. Most notably, the film cooling hole at the bottom of the contour plot shows increased coolant flow and jet spreading downstream compared to the other three holes. A closer inspection revealed that this hole had more of the cork removed

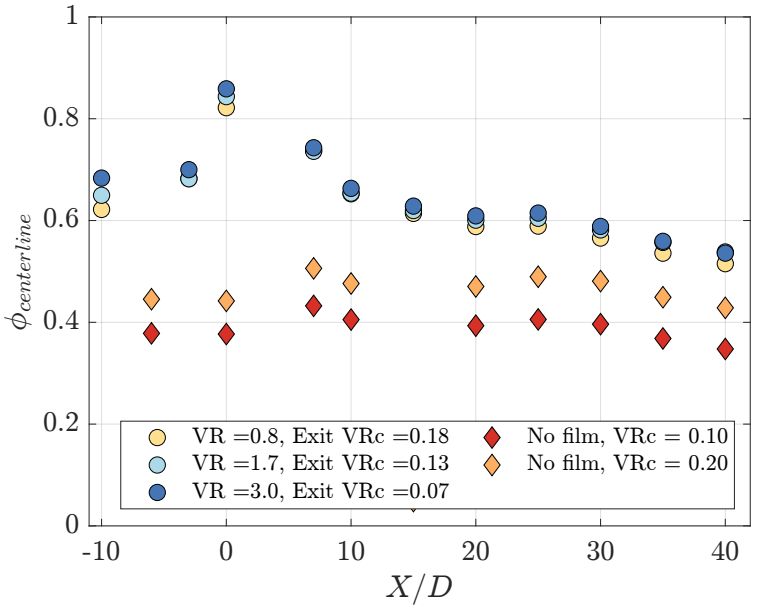

(a) Smooth Channel

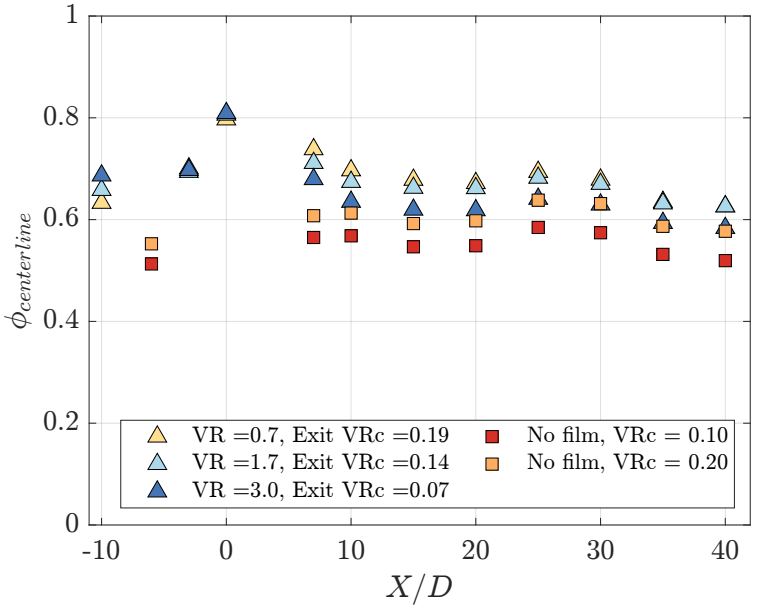

(b) Ribbed Channel

Figure 4.12: Centerline effectiveness for a smooth and turbulated channel, with and without film cooling.

around the outlet, effectively giving it a wider expansion angle than the neighboring holes. Due to the uncertainty associated with measuring a small difference in flow rates, discharge coefficient measurements were not obtained for each individual hole.

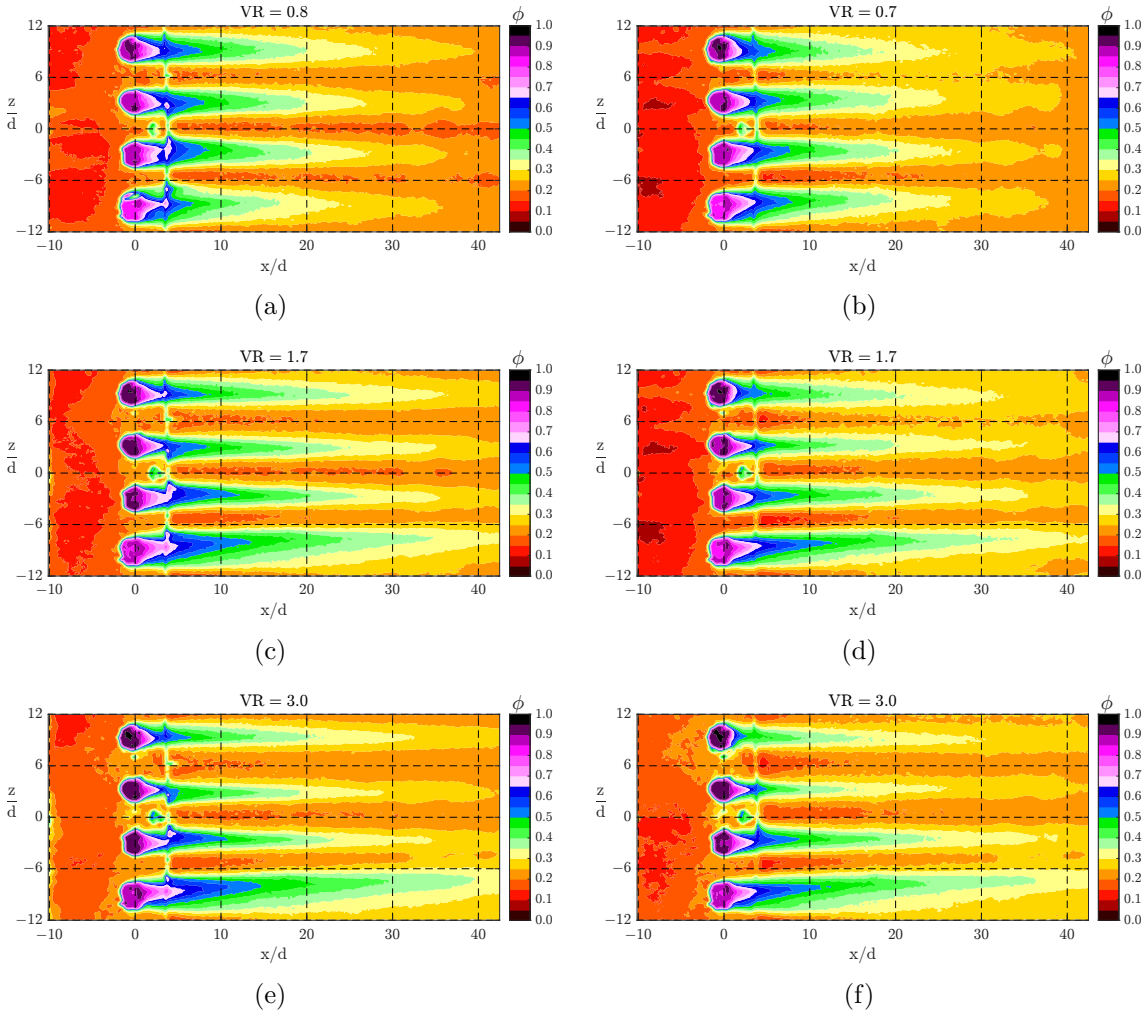

Figure 4.13: Contours of overall effectiveness ϕ on the TBC surface for the $15-15-1$ film cooling hole fed by a smooth (left) and turbulated (right) co-flow channel velocity ratio of $VR_c = 0.20$.

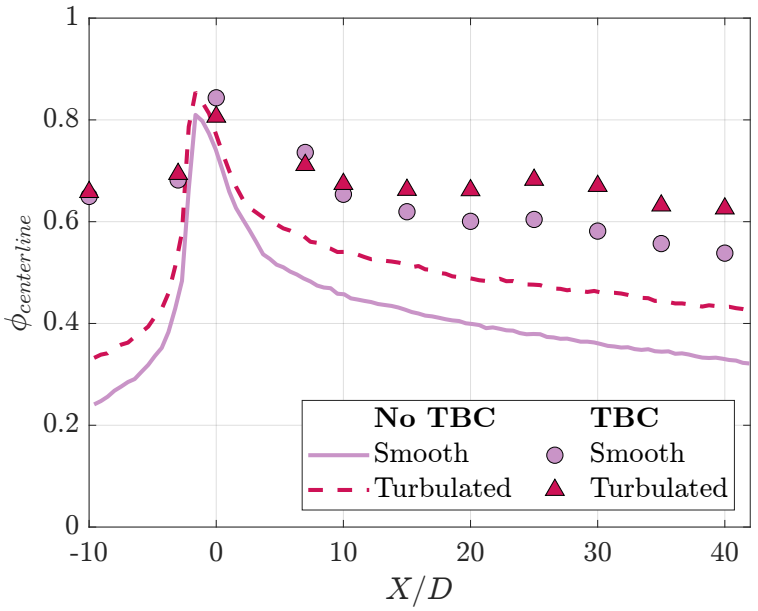

Figure 4.14: Comparison of centerline effectiveness for film cooling designs with and without a TBC.

Figure 4.14 shows the effect of a TBC on film-cooled designs. The effect of bore cooling is significantly enhanced upstream of the holes, where the smooth channel cases with a TBC show a 170% improvement in ϕ compared to the metal alone for VR = 1.7 at X/D = -10. The effectiveness gradient near the hole with a TBC is significantly reduced, which would correspond to lower thermal stresses in an actual engine and lead to improved part lifetime. The effect of channel design on overall effectiveness appears to be independent of the presence of a TBC as the smooth and ribbed channels show a similar difference in performance downstream of the film cooling holes.

4.4.2 Computational Results

The RANS analysis with a TBC showed greater deviation from the experimental data than the cases without a TBC. Figure 4.15 shows a comparison of the centerline effectiveness, indicating that the CFD over-predicts the performance of the overall design. For both the experimental and computational results, the VR = 0.8 case shows the lowest effectiveness. The computational results indicate a performance decrease after VR = 1.67, whereas the experimental effectiveness is relatively stable.

For the turbulated channel with TBC, shown in Figure 4.16, the computational results show a larger deviation from the experimental results and do not capture the trends well. The centerline effectiveness decreases with increasing VR, whereas the CFD predicts a small increase in performance before falling off. A cause of this discrepancy could be the fact that the RANS analysis assumed a "perfect" TBC application, meaning that the opening in the TBC was a continuous extension of the film cooling hole geometry at the same expansion angles. This was not the case for the experimental geometry or representative of actual engine conditions where the TBC is sprayed on the external surface. The imperfections in the hole outlet could have contributed to reduced experimental performance compared to the computational effectiveness. This effect can be seen in Figure 4.13.

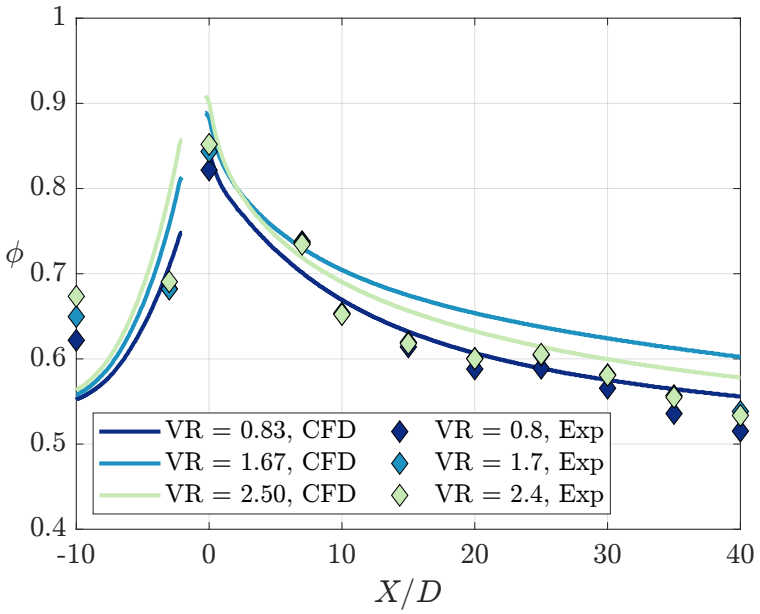

Figure 4.15: Centerline effectiveness for smooth channel on TBC-metal interface.

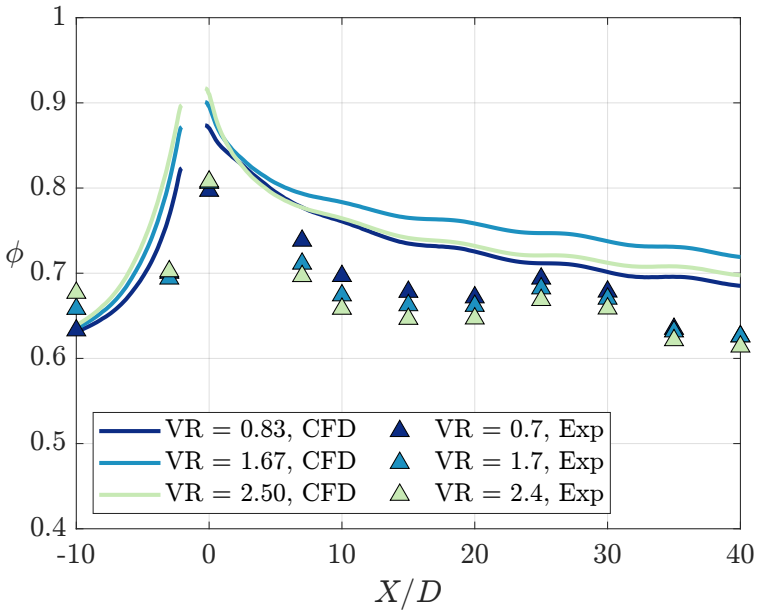

Figure 4.16: Centerline effectiveness for turbulated channel on TBC-metal interface.

4.5 Computational Insights

Although the computational analysis was not able to exactly predict the effectiveness for all cases tested, it is a valuable engineering tool that can provide insights into the system that are not easily obtained experimentally. Figure 4.17 shows the full effectiveness map on the simulated TBC-metal interface, which was not obtained experimentally. While the film jet on the TBC surface shows similar behavior for the smooth and turbulated channel, the effectiveness contours on the metal surface show a degradation in effectiveness downstream of the film cooling holes for smooth channel at higher velocity ratios corresponding to greater extraction ratios.

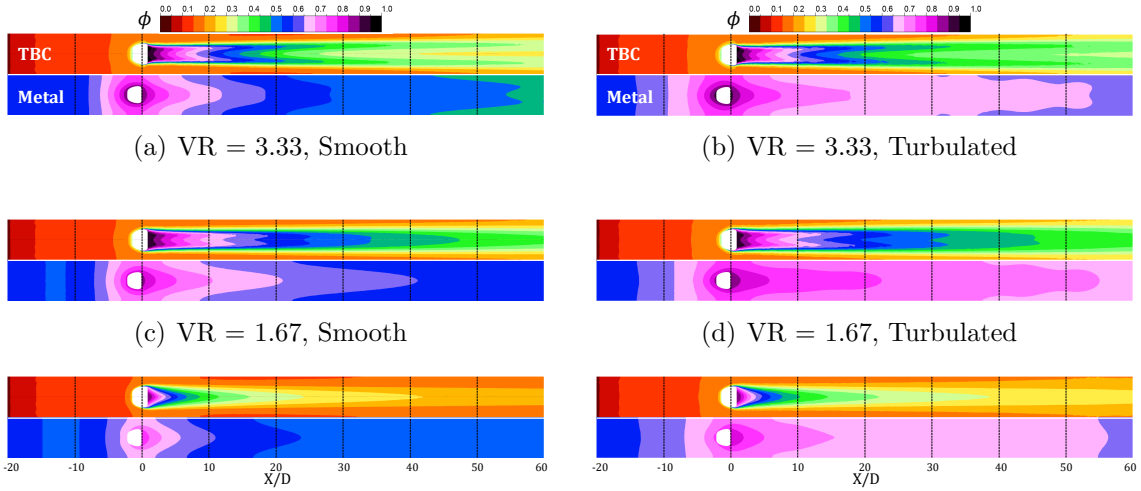

(a) VR = 3.33, Smooth

(b) VR = 3.33, Turbulated

(c) VR = 1.67, Smooth

(d) VR = 1.67, Turbulated

(e) VR = 0.42, Smooth

(f) VR = 0.42, Turbulated

Figure 4.17: Effectiveness of one film cooling hole pitch τ (top) and ϕ (bottom)

Figure 4.18 offers insight into the temperature distribution through the solid materials. While the turbulated channel without a TBC shows a similar θ distribution downstream of the film cooling holes to the smooth channel with a TBC, the effect of

bore cooling is significantly enhanced upstream of the holes. The TBC layer reduces the thermal gradients significantly. Localized changes in θ are observed near each individual rib location, which would not be seen if the heat transfer enhancement was due to a uniform surface roughness from an additive manufacturing process. A noticeable change in θ in the coolant channel is observed for both of the cases with ribs, as the coolant removes more thermal energy from the metal.

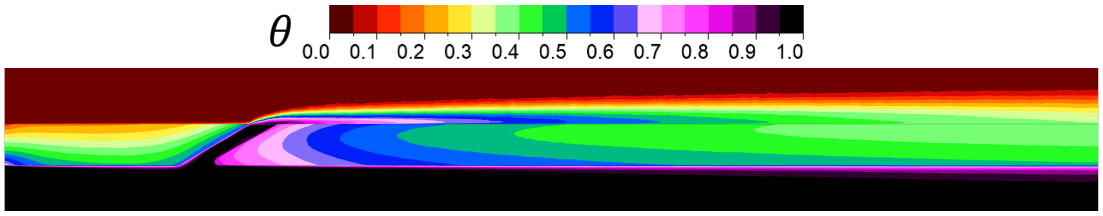

(a) Smooth channel without TBC

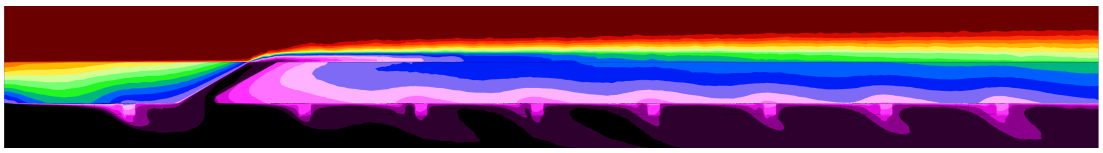

(b) Turbulated Channel without TBC

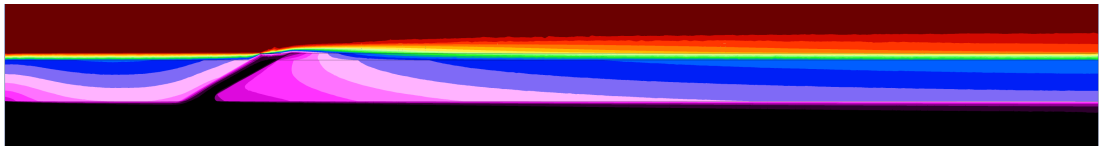

(c) Smooth Channel with TBC

(d) Turbulated Channel with TBC

Figure 4.18: Nondimensional temperature θ profiles on the hole centerline plane at VR = 1.67.

Chapter 5

Conclusion

5.1 Summary of Work

This study measured the overall effectiveness of film cooling, enhanced internal cooling, and the effects of an applied thermal barrier coating on a flat-plate matched-Biot number model. A key aspect of the study focused on the relationship between increased film cooling and decreased internal cooling effectiveness. A RANS conjugate heat transfer analysis was performed using ANSYS Fluent and compared to the experimental results. Adiabatic effectiveness measurements isolated the film performance from the overall effectiveness results. The key findings from this study are summarized below:

- Adiabatic effectiveness measurements of the 15-15-1 laidback fan-shaped hole fed by a smooth co-flow channel at $VR_c = 0.20$ showed increasing performance with increasing velocity ratio from VR = 0.7-1.7, and relatively constant performance from VR = 1.7-3.0.

- Without a TBC or film cooling, the addition of rib turbulators in a co-flow channel at $VR_c = 0.2$ improved spatially-averaged effectiveness by $\Delta\bar{\bar{\phi}} = 0.10$ from 0.22 to 0.32.

- The optimum velocity ratio for film cooling holes will be lower when enhanced internal cooling mechanisms are utilized. For the configurations tested, the increased film performance did not outweigh the reduction of internal cooling effectiveness. The turbulated channel showed a reduction in effectiveness above VR = 1.7, while the smooth channel design showed similar performance between VR = 1.7-3.0.

- The addition of a TBC to an internal cooling design provided an increase of $\Delta\bar{\bar{\phi}}$ = 0.25 for a smooth channel and $\Delta\bar{\bar{\phi}}$ = 0.28 for the turbulated channel.

- For film-cooled designs, the optimum VR decreased to VR = 1.1 for a turbulated channel. Cooling effects through the bore of the hole were enhanced significantly with the addition of a TBC.

- The RANS analysis closely predicted the thermal performance of the designs without a TBC, but over-predicted the effectiveness on the TBC-metal surface. Possible causes include deformities in the experimental film cooling hole exits that were not present in the computational analysis.

5.2 Conclusions

This study shows that for a constant amount of coolant, there is a balance between film cooling and enhanced internal convective cooling in turbine component thermal protection designs. For all cases tested, the designs with film cooling performed better than or equal to those with internal cooling alone, even with a TBC and enhanced internal cooling. Configurations with rib turbulators performed better

at VR = 1.7 than at VR = 3.0 as the downstream coolant channel had a higher VR_c and the adiabatic effectiveness measurements showed little change in $\bar{\eta}$ above VR = 1.7. The addition of a thermal barrier coating further reduced the optimum velocity ratio, although film cooling still provided a benefit. The deformities at the outlet of film cooling holes with a TBC can significantly alter the film effectiveness on the TBC surface and should be considered as part of the overall analysis. There is not a single answer for the optimum cooling configuration for all components as the exact design would depend on the maximum temperature limits, heat load, and coolant mass flow rate and pressure driver available at each location.

5.3 Recommendations for Future Work

As additive manufacturing becomes increasingly viable for production turbine components, the design space for thermal protection geometries will expand significantly. Numerical optimization of film cooling hole designs, such as the method discussed in [14], would be valuable in determining an improved coolant extraction method for designs incorporating a TBC, with the understanding that the best configuration with TBC may be significantly different from traditional film cooling designs. In determining an objective function, the effects upstream of the extraction location should be noted as well to take into account the significant contribution of bore cooling to the overall effectiveness.

Bibliography

[1] *Annual energy outlook 2019*. Summary Report AEO2019. U.S. Energy Information Administration, 2019.

[2] *FAA aerospace forecast*. Summary Report TC20-0011. Federal Aviation Administration, 2020.

[3] Lee S. Langston. Powering Out of Trouble. *ASME Mechanical Engineering Magazine*, 135(12):36–41, 12 2013.

[4] J. Dahl. File:jet engine.svg. `https://commons.wikimedia.org/wiki/File:Jet_engine.svg`, December 2007. Online; accessed 27 September 2020.

[5] Michael J. Moran, Howard N. Shapiro, Daise D. Boettner, and Margaret B. Bailey. *Fundamentals of Engineering Thermodynamics*. John Wiley & Sons, Hoboken, NJ, eighth edition, 2014.

[6] Douglas Quattrochi. Brayton cycle. `http://web.mit.edu/16.unified/www/SPRING/propulsion/notes/node27.html`, August 2006. Online; accessed 12 October 2020.

[7] Frank J. Cunha. 4.4.1 Heat Transfer Analysis. In *The Gas Turbine Handbook*. National Energy Technology Laboratory, U.S. Department of Energy, 2006.

[8] Ronald S. Bunker. Evolution of Turbine Cooling. In *ASME Turbo Expo 2017: Power for Land, Sea, and Air*, page V001T51A001, Charlotte, North Carolina, USA, June 2017. American Society of Mechanical Engineers.

[9] Kathryn L. Kirsch and Karen A. Thole. Experimental Investigation of Numerically Optimized Wavy Microchannels Created Through Additive Manufacturing. *Journal of Turbomachinery*, 140(2):021002, February 2018.

[10] Curtis K. Stimpson, Jacob C. Snyder, Karen A. Thole, and Dominic Mongillo. Roughness Effects on Flow and Heat Transfer for Additively Manufactured Channels. *Journal of Turbomachinery*, 138(5):051008, May 2016.

[11] David G. Bogard and Karen A. Thole. Gas Turbine Film Cooling. *Journal of Propulsion and Power*, 22(2):249–270, 2006.

[12] Ronald S. Bunker. The Effects of Manufacturing Tolerances on Gas Turbine Cooling. *Journal of Turbomachinery*, 131(4):041018, October 2009.

[13] Robert P. Schroeder and Karen A. Thole. Adiabatic Effectiveness Measurements for a Baseline Shaped Film Cooling Hole. In *ASME Turbo Expo 2014: Power for Land, Sea, and Air*, page V05BT13A036, Düsseldorf, Germany, June 2014. American Society of Mechanical Engineers.

[14] Fraser B. Jones III. *Investigation of Inlet and Diffuser Geometry Modifications on Film Cooling Performance of Additively Manufactured Shaped Holes in Crossflow.* PhD thesis, University of Texas at Austin, Austin, TX, 2020.

[15] Fraser B. Jones III and David G. Bogard. Parametric Optimization of Film Cooling Hole Geometry. In *ASME Turbo Expo 2021: Power for Land, Sea, and Air*, June 2021.

[16] Jason E. Dees, David G. Bogard, Gustavo A. Ledezma, Gregory M. Laskowski, and Anil K. Tolpadi. Experimental Measurements and Computational Predictions for an Internally Cooled Simulated Turbine Vane. *Journal of Turbomachinery*, 134(6):061003, November 2012.

[17] Curtis K. Stimpson, Jacob C. Snyder, Karen A. Thole, and Dominic Mongillo. Effectiveness Measurements of Additively Manufactured Film Cooling Holes. *Journal of Turbomachinery*, 140(1):011009, January 2018.

[18] S. M. Meier and D. K. Gupta. The Evolution of Thermal Barrier Coatings in Gas Turbine Engine Applications. *Journal of Engineering for Gas Turbines and Power*, 116(1):250–257, January 1994.

[19] William R. Stewart, David A. Kistenmacher, and David G. Bogard. Effects of TBC Thickness on an Internally and Film Cooled Model Turbine Vane. In *ASME Turbo Expo 2014: Power for Land, Sea, and Air*, page V05BT13A058, Düsseldorf, Germany, June 2014. American Society of Mechanical Engineers.

[20] S. Na, B. Williams, R. A. Dennis, K. M. Bryden, and T. I.-P. Shih. Internal and Film Cooling of a Flat Plate With Conjugate Heat Transfer. In *ASME Turbo Expo 2007: Power for Land, Sea, and Air*, pages 545–554, Montreal, Canada, January 2007. American Society of Mechanical Engineers.

[21] Jonathan Maikell, David Bogard, Justin Piggush, and Atul Kohli. Experimental Simulation of a Film Cooled Turbine Blade Leading Edge Including Thermal Barrier Coating Effects. *Journal of Turbomachinery*, 133(1):011014, January 2011.

[22] F. Todd Davidson, Jason E. Dees, and David G. Bogard. An Experimental Study of Thermal Barrier Coatings and Film Cooling on an Internally Cooled Simulated Turbine Vane. In *ASME Turbo Expo 2011: Power for Land, Sea, and Air*, pages 559–570, Vancouver, British Columbia, Canada, January 2011. ASMEDC.

[23] F. Todd Davidson, David A. KistenMacher, and David G. Bogard. Film Cooling With a Thermal Barrier Coating: Round Holes, Craters, and Trenches. *Journal of Turbomachinery*, 136(4):041007, April 2014.

[24] J. C. Han, Y. M. Zhang, and C. P. Lee. Augmented Heat Transfer in Square Channels With Parallel, Crossed, and V-Shaped Angled Ribs. *Journal of Heat Transfer*, 113(3):590–596, August 1991.

[25] NASA Glenn Research Center. Air viscosity: Sutherland's formula. `https://www.grc.nasa.gov/www/BGH/viscosity.html`, 2004. Online; accessed 26 October 2020.

[26] T.-H. Shih, W.W. Liou, A. Shabbir, Z. Yang, and J. Zhu. A New k-e Eddy Viscosity Model for High Reynolds Number Turbulent Flows-Model Development and Validation. NASA Technical Memorandum 106721, 1994.

[27] Fraser B. Jones, Dale W. Fox, and David G. Bogard. Evaluating the Usefulness of RANS in Film Cooling. In *ASME Turbo Expo 2019: Power for Land, Sea, and Air*, page V05AT12A019, Phoenix, Arizona, USA, June 2019. American Society of Mechanical Engineers.

[28] W.L. Oberkampf and C.J. Roy. *Verification and Validation in Scientific Computing*. Cambridge University Press, 2010.

[29] Joshua B Anderson. *Investigation of Approach Flow Parameters, Scaling Factors, and Measurement Accuracy for Film Cooling Effectiveness and Heat Transfer Coefficient Measurements*. PhD thesis, The University of Texas at Austin, August 2017.

[30] Theodore L. Bergman, Adrienne S. Lavine, Frank P. Incropera, and David P. Dewitt. *Fundamentals of Heat and Mass Transfer*. John Wiley & Sons, Hoboken, NJ, seventh edition, 2011.

[31] TCPoly. Technial datasheet: Ice9 rigid. `https://tcpoly.com/wp-content/uploads/2020/08/TDS_ice9_Rigid.pdf`, August 2020. Online; accessed 1 September 2020.

[32] D.C. Montgomery and G.C. Runger. *Applied Statistics and Probability for Engineers*. John Wiley & Sons, 2010.

[33] Robert J. Moffat. Describing the uncertainties in experimental results. *Experimental Thermal and Fluid Science*, 1(1):3–17, January 1988.

[34] Dale W. Fox, Fraser B. Jones, John W. McClintic, David G. Bogard, Thomas E. Dyson, and Zachary D. Webster. Rib Turbulator Effects on Crossflow-Fed Shaped Film Cooling Holes. *Journal of Turbomachinery*, 141(3):031013, March 2019.

[35] M. Gritsch, C. Saumweber, A. Schulz, S. Wittig, and E. Sharp. Effect of Internal Coolant Crossflow Orientation on the Discharge Coefficient of Shaped Film-Cooling Holes. *Journal of Turbomachinery*, 122(1):146–152, January 2000.

[36] M. Gritsch, A. Schulz, and S. Wittig. Discharge Coefficient Measurements of Film-Cooling Holes With Expanded Exits. In *ASME Turbo Expo 1997: Power for Land, Sea, and Air*, page V003T09A030, Orlando, Florida, USA, June 1997.

[37] R. B. Dean. Reynolds Number Dependence of Skin Friction and Other Bulk Flow Variables in Two-Dimensional Rectangular Duct Flow. *Journal of Fluids Engineering*, 100(2):215–223, June 1978.

[38] Jason E Albert. *Experimental Simulation and Mitigation of Contaminant Deposition on Film Cooled Gas Turbine Airfoils*. PhD thesis, The University of Texas at Austin, May 2011.

[39] Cynthia A. Brewer. Colorbrewer 2.0. `https://colorbrewer2.org/`.

Vita

Matthew Jeffrey Horner grew up in Walnut Creek, California, where he attended Las Lomas High School. He earned his B.S. from the University of California - Los Angeles in Mechanical Engineering and graduated *magna cum laude* in 2019. While at UCLA, he was a four-year student athlete on the Varsity Rowing Team and a member of the Tau Beta Pi engineering honor society. He began graduate studies at the University of Texas at Austin in fall of 2019 and joined Dr. David Bogard's Turbulence and Turbine Cooling Research Lab. After graduation in December 2020 with a Master of Science in Mechanical Engineering, he will be working as a Mechanical Design Engineer at Solar Turbines in San Diego, California.

Permanent email address: mjhorner@ucla.edu

This thesis was typeset by the author using LaTeX.